AD_____

Award Number:W81XWH-08-1-0261

TITLE:3D Facial Pattern Analysis for Autism

PRINCIPAL INVESTIGATOR: Ye Duan, Ph.D

CONTRACTING ORGANIZATION:University of Missouri, Columbia, MO 65211

REPORT DATE: July 2010

TYPE OF REPORT: Final

PREPARED FOR: U.S. Army Medical Research and Materiel Command
Fort Detrick, Maryland 21702-5012

DISTRIBUTION STATEMENT:

X Approved for public release; distribution unlimited

The views, opinions and/or findings contained in this report are those of the author(s) and should not be construed as an official Department of the Army position, policy or decision unless so designated by other documentation.

REPORT DOCUMENTATION PAGE

Form Approved
OMB No. 0704-0188

Public reporting burden for this collection of information is estimated to average 1 hour per response, including the time for reviewing instructions, searching existing data sources, gathering and maintaining the data needed, and completing and reviewing this collection of information. Send comments regarding this burden estimate or any other aspect of this collection of information, including suggestions for reducing this burden to Department of Defense, Washington Headquarters Services, Directorate for Information Operations and Reports (0704-0188), 1215 Jefferson Davis Highway, Suite 1204, Arlington, VA 22202-4302. Respondents should be aware that notwithstanding any other provision of law, no person shall be subject to any penalty for failing to comply with a collection of information if it does not display a currently valid OMB control number. **PLEASE DO NOT RETURN YOUR FORM TO THE ABOVE ADDRESS.**

1. REPORT DATE *(DD-MM-YYYY)*
01-07-2010

2. REPORT TYPE
Final

3. DATES COVERED *(From - To)*
1 JUL 2008 - 30 JUN 2010

4. TITLE AND SUBTITLE
3D Facial Pattern Analysis for Autism

5a. CONTRACT NUMBER

5b. GRANT NUMBER
W81XWH-08-1-0261

5c. PROGRAM ELEMENT NUMBER

6. AUTHOR(S)
Ye Duan

5d. PROJECT NUMBER

5e. TASK NUMBER

5f. WORK UNIT NUMBER

7. PERFORMING ORGANIZATION NAME(S) AND ADDRESS(ES)
University of Missouri, Columbia, MO 65211

8. PERFORMING ORGANIZATION REPORT NUMBER

9. SPONSORING / MONITORING AGENCY NAME(S) AND ADDRESS(ES)
U.S. Army Medical Research and Materiel Command
Fort Detrick, Maryland 21702-5012

10. SPONSOR/MONITOR'S ACRONYM(S)

11. SPONSOR/MONITOR'S REPORT NUMBER(S)

12. DISTRIBUTION / AVAILABILITY STATEMENT
Approved for public release; distribution unlimited

13. SUPPLEMENTARY NOTES

14. ABSTRACT

The goal of this project is to use recently developed 3D shape acquisition technologies and advanced computational techniques to define the autism face and determine whether there is a statistically significant facial phenotype.

During this report period, we had generated a set of precise, highly replicable 3D anthropometric data for core ASD children and age-matched, typically developing controls, which has not previously been done. We had conducted 3D and 2D facial pattern analysis and study results suggest that there are subgroups of individuals with ASD that display distinct facial phenotypes.

15. SUBJECT TERMS
Phenotype, Autism, Facial pattern analysis.

16. SECURITY CLASSIFICATION OF:			**17. LIMITATION OF ABSTRACT**	**18. NUMBER OF PAGES**	**19a. NAME OF RESPONSIBLE PERSON**
					USAMRMC
a. REPORT	**b. ABSTRACT**	**c. THIS PAGE**	UU	50	**19b. TELEPHONE NUMBER** *(include area code)*
U	U	U			

Standard Form 298 (Rev. 8-98)
Prescribed by ANSI Std. Z39.18

Table of Contents

	Page
Introduction……..…..	**1-1**
Body……..	**2-14**
Key Research Accomplishments……..	**15-15**
Reportable Outcomes……	**16-16**
Conclusion……	**17-17**
References……	**18-18**
Appendices……	**19-47**

Introduction

This project will address whether the core group of idiopathic autism, often called essential autism is neurodevelopmental. We have observed clinically that children in the core population have a common facial gestault, which can be described as physically pleasing with wide spaced, deep set eyes and a broad forehead. The phenotype is subtle, not generally outside 2SD, so not easily catagorized by standard measurements. Study of this facial gestault is considered potentially informative since children with complex ASDs are often hyperteloric and facial dysmorphogeneis can serve as an index of brain dysmorphogenesis. This project will use recently developed 3D shape acquisition technologies and advanced computational techniques to define the autism face and determine whether there is a statistically significant facial phenotype.

Body

Overview

We had finished all the proposed tasks proposed in this project (07/01/2008 to 06/30/2010) in the statement of work. We had conducted 2D and 3D facial pattern analysis. In the following, we will describe each of the finished tasks in details.

TASK 1: 3DMD® cranial system procurement and installation

We had obtained $100,000 internal funding from our university and had purchased the 3DMD® cranial system (Figure 1) for this project. It is currently installed in the Thompson Center for Autism in University of Missouri.

Figure 1: 3DMD® cranial system (http://www.3dmd.com/).

TASK 2: Subjects/Controls recruiting and selection

We had obtained IRB approval for our project, and had recruited 40 subjects and 72 age-matched, typically developing controls. The subjects are recruited from our large clinic population in the Thompson Center for Autism in University of Missouri. The age range is between 8 to 12 years old.

TASK 3: 3D surface data acquisition and facial feature extraction

We conducted full 360 degree head/face scan using the 3DMD® cranial system for all the subjects and controls recruited for the project. A 3D surface model with both the geometry and the co-registered texture image is obtained for each subject (Figure 2).

(a)

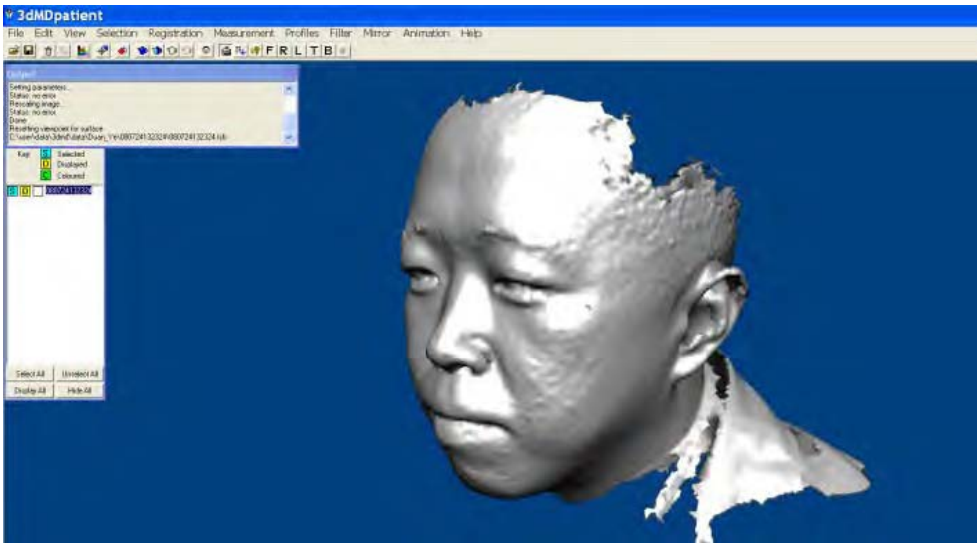

(b)

Figure 2: An example of the 3D surface model of the PI with both the geometry (b) and the co-registered texture image (a) obtained using the 3DMD® cranial system.

After the 3D face scan, we use the 3DMD patient® software to obtain 3D coordinate data for a suite of anthropometric facial landmarks (Figure 2), following [1]. Figure 3 shows an example of using the 3DMD patient® software to calculate the intercanthal distance between landmarks "en-en" of Figure 2.

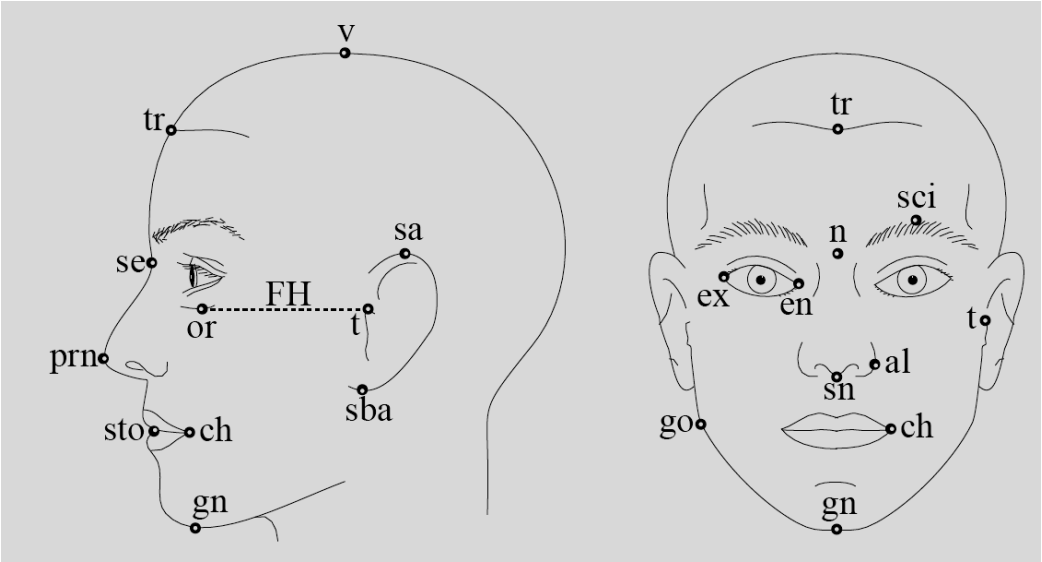

Figure 2: Anthropometric landmarks and measurements on face [1].

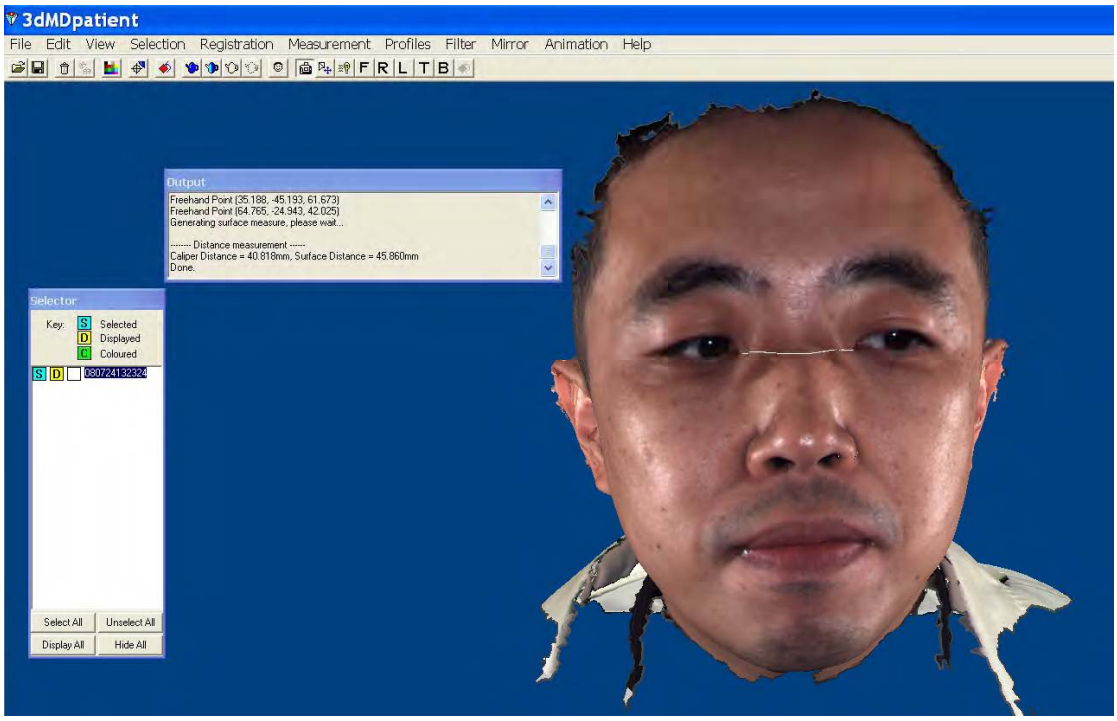

Figure 3: An example of measuring the distances between anthropometric facial landmarks defined in [1] using the 3DMD patient® software. Here the intercanthal distance between landmarks "en-en" (Figure 2) is measured.

TASK 4: Facial phenotype exploration and correlation with clinical observations

1. 3D facial pattern analysis:

We had conducted 3D facial pattern analysis for facial phenotype exploration. The research result has been published in [4]. We collected 19 anthropometric landmarks (Table 1) from the 3dMD images from all individuals with the observer blinded to clinical diagnosis. We use a form of principal coordinates analysis (PCOORD), which is a clustering method developed specifically for landmark data [2]. This analysis enables investigation of how salient features of facial anatomy combine on a multivariate axis to define similarities (and dissimilarities) among shapes. The goal is to identify the specific combination of morphological variables that successfully separate individuals into groups by projecting them onto the multivariate space. The computational details of principal coordinates analysis can be found in Krzanowski [3].

Phenotype	Anthropometric measurement
Broad forehead	ft-ft; ft-ft / tr-g
Wide nasal bridge	en-en / al-al
Hypertelorism	en-en; en-en / t-t; en-en / eu-eu
Almond-shaped eyes	en-ex / ps-pi
Wide philtrum	cph-cph; cph-cph / ch-ch
Pointed chin	go-gn / go-go; sn-gn / go-go
Outstanding helices	sa-sa /t-t

Table 1 - anthropometric landmarks facial features studied in this project.

We performed PCOORD analysis on the anthropometric data collected from the faces of the 29 individuals with ASD for whom we have completed data collection. In order to control for effects of size, each individual's data were scaled by the geometric mean of all possible linear distances between landmarks, following. The first two principal axes are illustrated in Figure 4. The first and second principal axes account for approximately 19.12% and 17.88% of the variation within the study sample, respectively. Note that several individuals on the high negative end of the first axis and high positive end of the second axis cluster separately from the main group overall (top left of Figure 4a). Suites of linear distances that are highly correlated with this location on these axes describe the shape of the mouth and the mouth's relative location within the face as a whole. These individuals display a wider philtrum and wider mouth overall relative to the rest of the face as compared to the remainder of the individuals in this sample. Also, the mouth is located in a more superior position relative to the upper and midface, such

that is closer to the nose. As the data have been scaled for size, this is not an effect of age or growth.

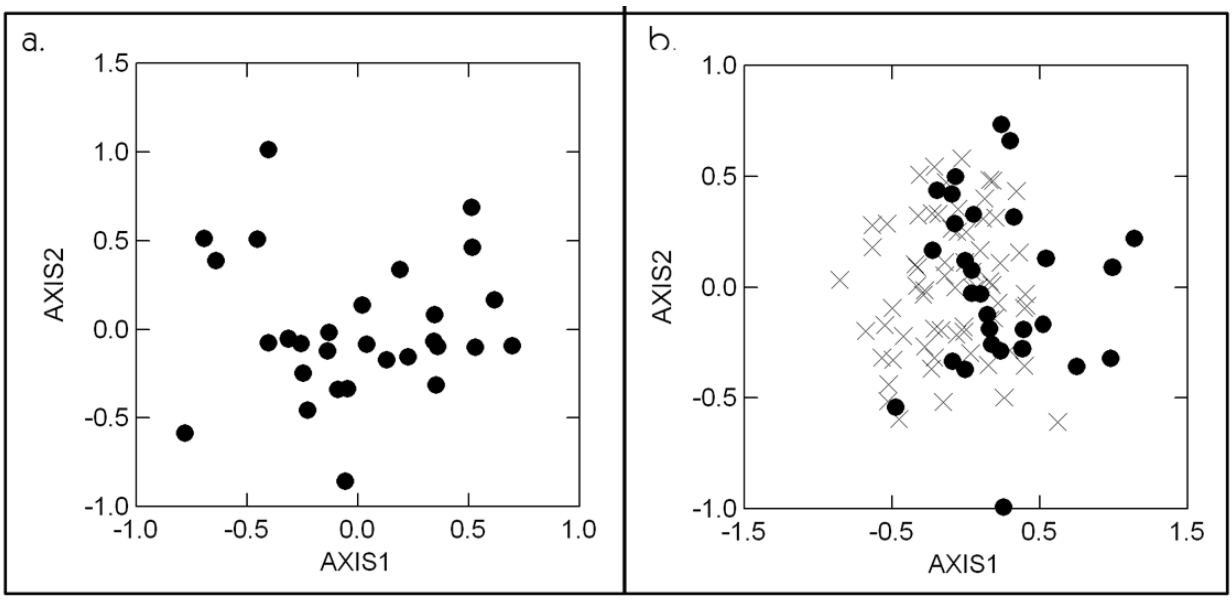

(a) (b)

Figure 4: Facial feature clustering result for ASD based on principal coordinates analysis (PCOORD). (a) is the clustering result within the ASD group, (b) is the clustering result by combining the ASD group (shown as dot) and the control group (shown as X) together. Only the first two principal axes are shown here. See text for more descriptions.

Though this subgroup of individuals appears to be outside of the range of phenotypes of the majority of the individuals in our sample, we cannot know from this analysis whether the individuals in the subgroup or the main group are more representative of the typically-developing facial phenotype. To answer this question we must include the same data for both individuals with ASD and typically-developing individuals. Thus, we performed the same PCOORD analysis with the 29 individuals with ASD and included in the analysis data acquired from 69 typically-developing individuals. These data were also scaled to control for the effects of size. The first two principal axes are illustrated in Figure 4b. First, the majority of individuals with ASD cluster together with the typically-developing individuals. However, we see several individuals located on the high positive end of the first axis, with this axis accounting for approximately 18.65% of the variation in the sample. Again, these data were scaled prior to analysis, which indicates that the distribution of individuals is not based on age- or growth-related differences; in fact, the individuals included in this cluster are the same individuals that clustered separately in the analysis of only the individuals with ASD. Additionally, the suites of linear distances that define this subgroup closely match those from the previous analysis, i.e., the breadth of the philtrum and mouth, and the more superiorly-located mouth.

The following are the summary of the study results:

1) Analyses show that children diagnosed with ASD demonstrate differences in facial morphology compared to typically developing children (Figure 5).

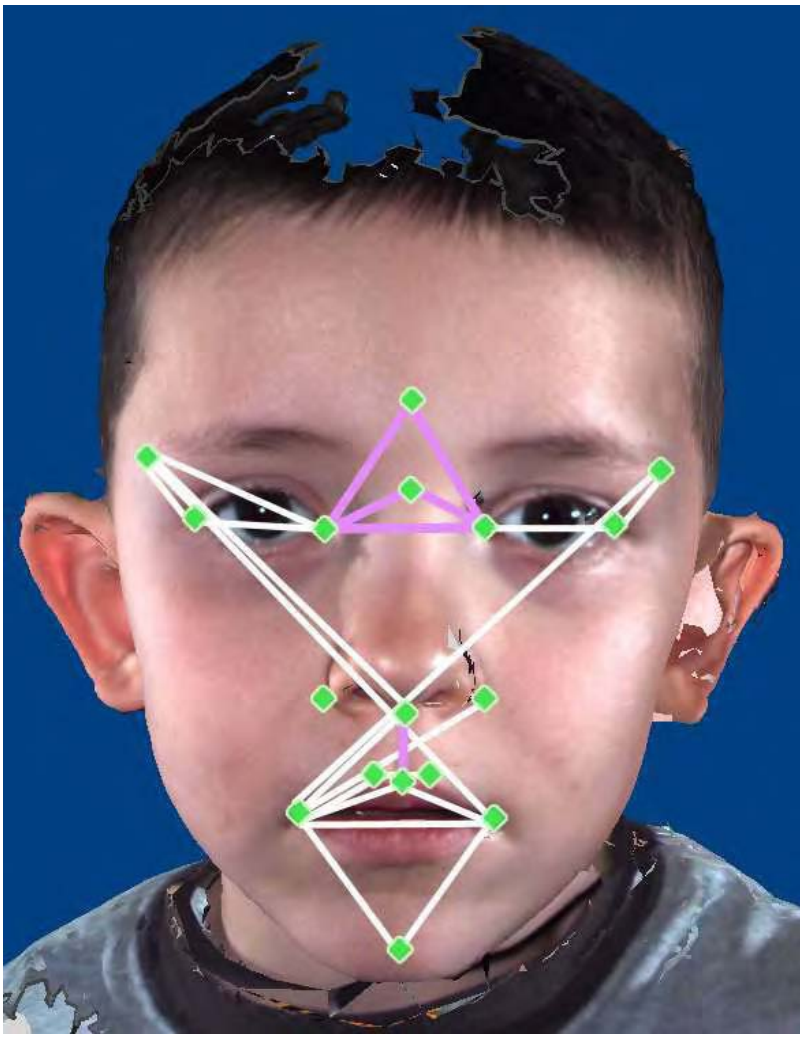

Figure 5: Measures that are significantly different in boys with ASD as compared to typically developing children. White lines indicate measures that are larger in children with ASD, while purple lines represent measures that are smaller in children with ASD.

2) There are 2 subgroups of children with ASD that are different from both the other children with ASD and typically developing children (Figure 6). These results do not reflect correlations with age or head size.

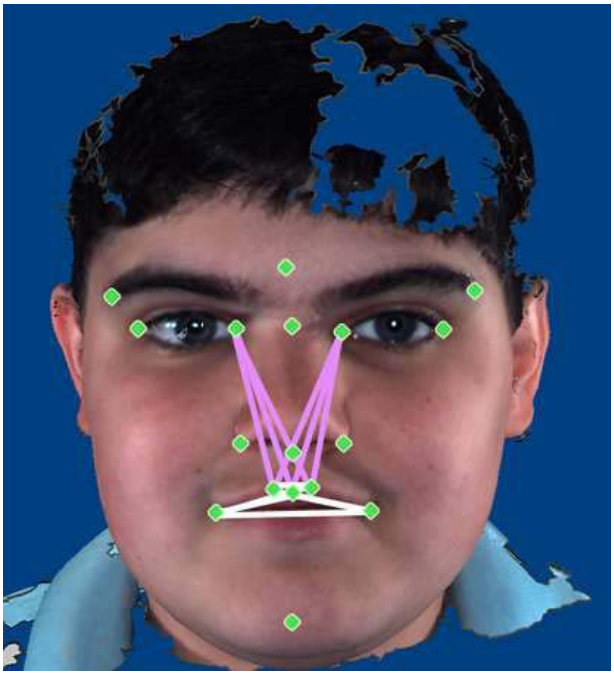

(a)

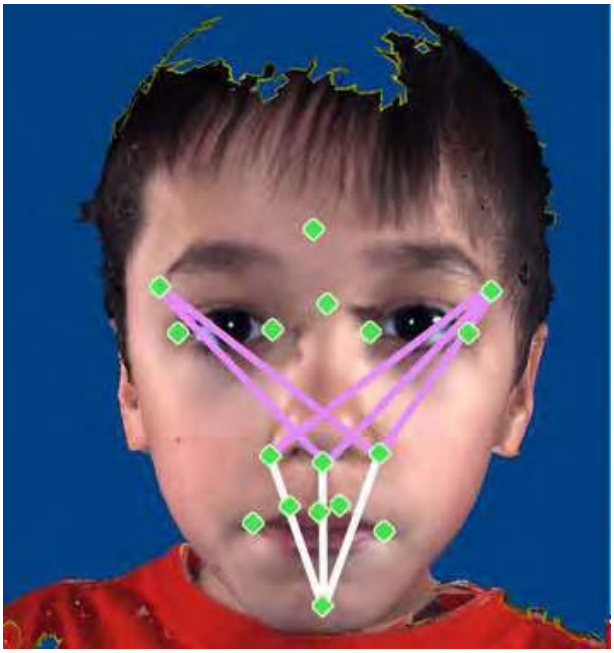

(b)

Figure 6: There are two subgroups within ASD. a) Measures distinguishing Subgroup 1. Purple lines indicate measures positively correlated with Axis 1, while white lines are negatively correlated with Axis 1. b) Measures distinguishing Subgroup 2. Purple lines indicate measures positively correlated with Axis 2, while white lines are negatively correlated with Axis 2.

3) We find statistically significant correlations between subgroup membership and clinical and behavioral characteristics (Table 1).

Table 1: Significant correlations with subgroup membership as compared to the main ASD group.

	Subgroup 1	Subgroup 2
Diagnosis	↑ Autistic Disorder	↑ Asperger's
Severity	High SCQ	Moderate SCQ
IQ	Lower	Higher
Attention	Higher CBCL	Lower CBCL
Language	----------	Higher
Family history	----------	↑Anxiety Disorder
Other	↑ seizures	↑ clumsiness

2. 2D facial pattern analysis:

In this study we aim at the following task based on the 2D facial features of each subject: to find if there is such MFP group and the homogeneous features shared in this group. Frontal facial images of 41 subjects with ASD are used in this study. Sixteen feature points are automatically located on each facial image using our newly developed method [5]. To ensure the accuracy of the feature point location, all the results are examined by a human operator, and manual adjustment can be made if the detected feature point is off its correct location. Procrustes analysis is used to align the points across all the subjects. Size difference is removed during Procrustes analysis. EDMA is performed which generated a pairwise distance matrix. The upper diagonal of this matrix is concatenated into a distance vector. k points has k(k-1)/2 pairwise distances.

Our interest is finding a homogeneous midline facial group (MFP) group in the whole population, while the rest of the population is of less interest and may be heterogeneous itself. A proper clustering method needs to be chosen in order to suit our application. Traditional clustering methods such as k-means may not be a good choice, since we do not have a good estimate of the number of clusters due to the lack of hypothesis of the non-MFP group. High dimensionality of the feature vectors may also cause problems for many clustering algorithms due to the curse of dimensionality. Many dimension reduction methods have been developed which include feature transformation and feature selection. Feature transformation represents the

data by a smaller number of new features, each being a combination of the original features. Information from irrelevant dimensions is preserved, which makes these methods ineffective when the clusters are masked by irrelevant dimensions. The combinations of the original features are also difficult to interpret. Feature selection selects the most relevant dimensions from all dimensions, but it may have difficult when clusters exist in different groups of dimensions (subspaces).

Subspace clustering is an extension of feature selection that attempts to find clusters in different subspaces. It appears as biclustering in the application of gene expression data, but subspace clustering and biclustering are essentially the same. It can cluster the observations and features at the same time, thus performing feature selection during clustering process. Subspace clustering suits our purpose well, because we are interested in not only looking for an MFP group, but also which features can distinguish MFP from non-MFP.

We use the software BiVisu to perform biclustering. The data are represented in a matrix, where each column is a feature dimension, and each row is an observation (subject).

Classification is performed if we are able to find an MFP group by clustering. The clustered data are divided into training and test data. LDA and SVM are used to train the classifier. Since our sample size is relatively small and the number of subjects in each group is uncertain, it is difficult to divide the data into training and test sets fairly. Instead, we use leave-one-out method each time and then calculate the average classification rate.

Eight subjects have open mouths in their images. Two data matrices are constructed for two alternative ways to remove the open mouth effect. The first data matrix contains 33 rows (subjects) and 120 columns (distances), with the 8 subjects excluded. The second data matrix contains 41 rows and 45 columns, with the 6 feature points on the mouth excluded. Next we will show the results of the first data matrix in detail, and later we will summarize the results of the other matrix.

There are several parameters to set. The minimum number of columns of each cluster is set to 20, the minimum number of the rows is set to 25% of the total number of rows, the maximum cluster overlap is set to 20%, and the noise level is set to 0.05. A noise level too high will group the entire data matrix into one bicluster, and a noise level too low will find no bicluster.

Multiplicative model is used and the result gives 8 biclusters. The bicluster with the highest correlation is selected as the most significant bicluster. 14 subjects and 34 features are grouped into this bicluster. The ratio map of a bicluster is defined as the elementwise ratio of each column to a reference column (e.g., 1st column) of this bicluster. Figure 7 shows the ratio maps of the selected bicluster. The similar patterns across rows indicate the coherence of this cluster. Note that in this experiment there are 33 subjects and 120 features total.

Assume that the subjects in the selected bicluster belong to MFP group. Figure 8 shows the feature points of each subject, with MFP subjects in red and non-MFP subjects in blue. The distances in this bicluster are also shown, where the red lines indicate the average distance is longer in MFP group. From this plot we find that the group differences lie mostly in the eyes and the area between the nose and the mouth. MFP group have shorter eye width, shorter distance between eyes and longer eye height.

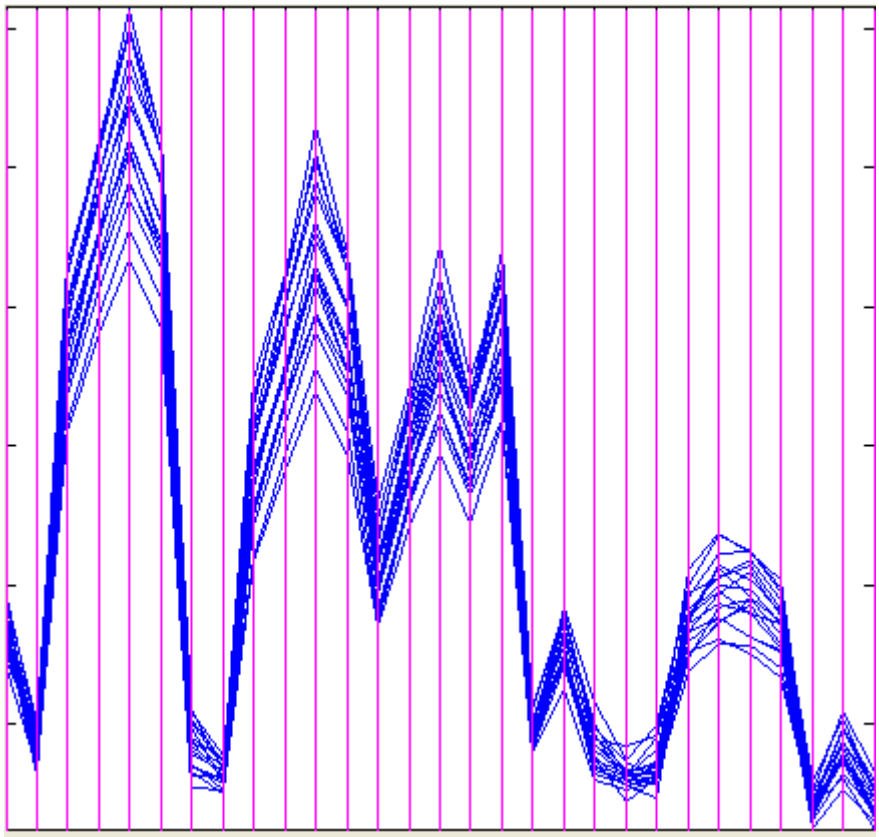

Figure 7: Ratio map of the bicluster for method 1.

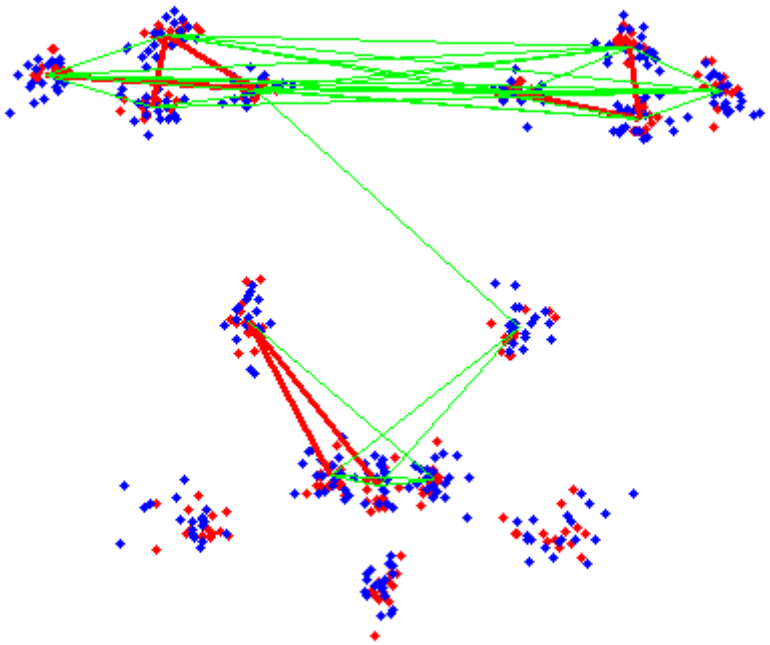

Figure 8: Feature points (red: MFP) and the selected pairwise distances (red: MFP>non-MFP) for method 1.

The data are labeled according to the clustering results, and only the 34 features in the selected bicluster are used in the classification. The experiment is performed 33 times, each time one subject being the test data. The average classification rate of LDA method is 84.8%, and the average rate of SVM is 60.6%.

Now we will show the results on the data set with 41 subjects and 10 feature points (45 features). Biclustering results give 4 biclusters, and the selected bicluster has 16 rows and 31 columns (Figure 9). Figure 10 is similar to Figure 8 except there are no mouth feature points. Compared with Figure 8, the same conclusion about the eye features can be drawn from Figure 10. However, the group difference of the eye-nose distance is inconsistent with Figure 8 and the nose width difference is not shown in Figure 8.

The classification is performed in the same way as 4.3. The average classification rate is 88.2% for LDA, and 72.3% for SVM.

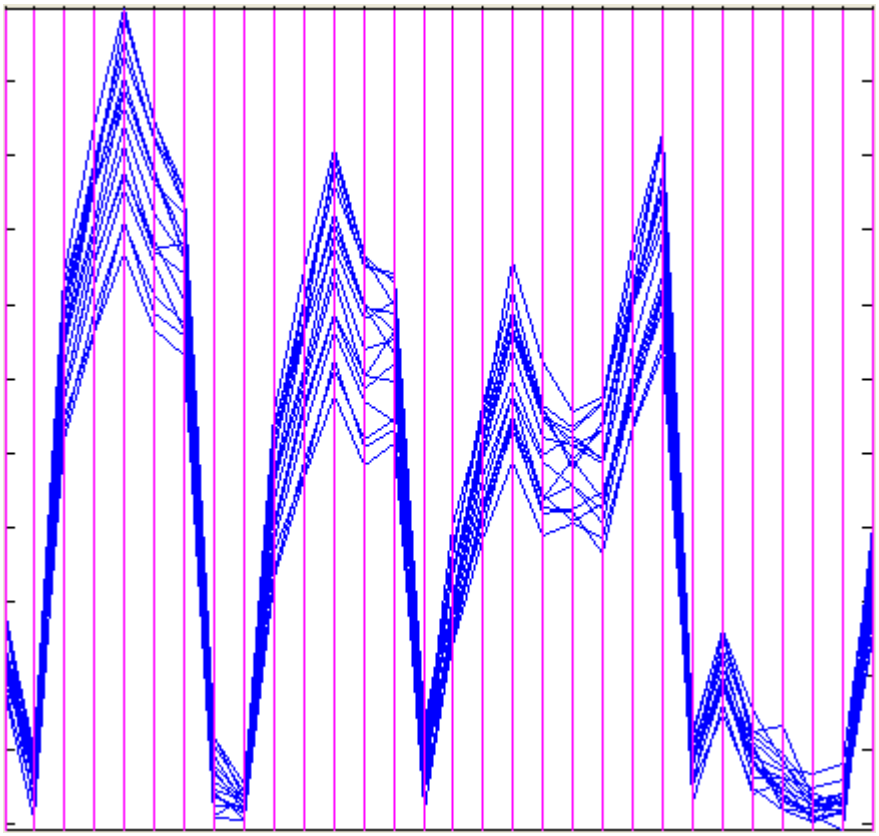

Figure 9: Ratio maps of the biclusters for method 2.

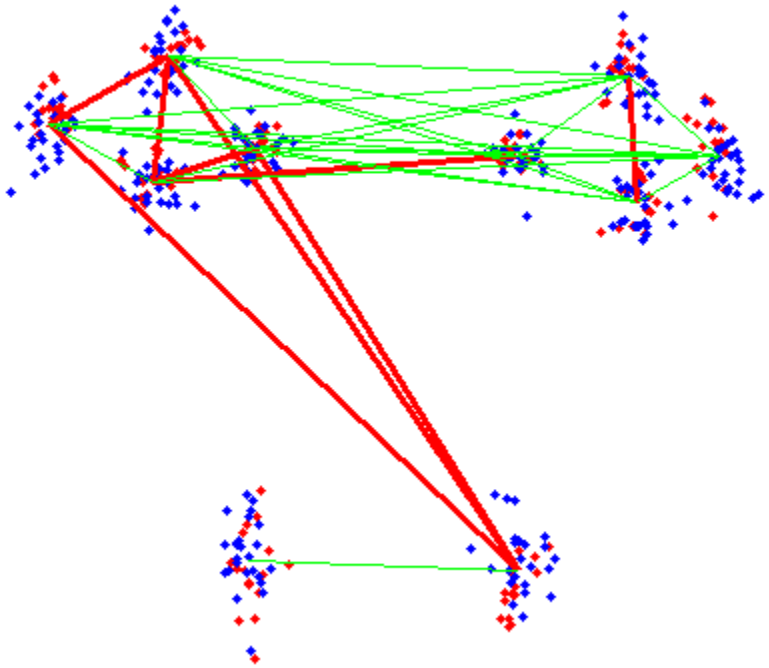

Figure 9:.Feature points (red: MFP) and the selected pairwise distances (red: MFP>non-MFP) for method 2.

Summary of Results:

We obtain two subgroups from the above results. The first is clustered from 33 subjects with 16 feature points (120 features), and the second is from 41 subjects with 10 feature points (45 features). By comparing the two groups, we find that they have 11 subjects in common, which constitute a majority of each group. Among the rest 5 subjects (16-11=5) in the second group, 3 of them are not included in the first experiment because of open mouth.

The two experiments select similar distances among eye feature points, and these distances show the same pattern of MFP group (shorter eye distance, longer eye height, etc). A few eye-nose distances are also selected in both experiments but the revealed patterns are inconsistent. This inconsistency is likely caused by the few non-overlapping subjects of the two MFP groups. Those subjects might be the noise in the corresponding clusters, although further experiment is needed to confirm it. Nose width is selected in the second experiment but not the first one, and several nose-mouth distances are selected in the first experiment only because of the exclusion of mouth feature points in the second experiment.

The subsequent classification is used to test if the selected features have the capability of distinguishing MFP from non-MFP. Both experiments show reasonable classification rates. LDA performs better than SVM although LDA is simpler in theory.

Based on what has been done so far, we find that there exists a homogeneous MFP group in the ASD population, and this group generally has shorter eye width, shorter eye distance and longer eye height compared to the rest of ASD population. Other facial features do not appear to be distinguishing in the subgroup, although further experiment is needed to provide more evidence.

Key Research Accomplishments

- We had generated a set of precise, highly replicable 3D anthropometric data for core ASD children and age-matched, typically developing controls, which has not previously been done.
- We had conducted 2D and 3D facial pattern analyses. Results suggest that there are subgroups of individuals with ASD that display distinct facial phenotypes.

Reportable Outcomes

- We had collected 3D surface model with both the geometry and the co-registered texture image is obtained for 40 ASD subjects and 72 age-matched, typically developing controls. We will make the data available for the public.
- Results of 3D and 2D facial pattern analyses suggest that there are subgroups of individuals with ASD that display distinct facial phenotypes.

Conclusion

We had generated a set of precise, highly replicable 3D anthropometric data for core ASD children and age-matched, typically developing controls, which has not previously been done. Results of 3D and 2D facial pattern analyses suggest that there are subgroups of individuals with ASD that display distinct facial phenotypes. Characterization of the facial phenotype will enhance understanding of embryologic forces which can cause autism, and may provide a potential prescreening tool to assist early diagnosis.

References

[1] Farkas L. Examination. In: Farkas L, editor. Anthropometry of the Head and Face, 2nd edition. New York: Raven Press, 1994: 3-56.

[2] Lele S, Richtsmeier J. 2001. An invariant approach to the statistical analysis of shapes. London: Chapman and Hall/CRC Press.

[3] Krzanowski W. 1988. Principles of multivariate analysis: a user's perspective. Oxford: Clarendon Press.

[4] Aldridge Kristina, Pope Kimberly, George Ian, Hill Cheryl, Takahashi Nicole, Miles Judith, Duan Ye. Facial Phenotypes and Subgroups in Children with Autism Spectrum Disorders. International Meeting for Autism Research (IMFAR) 2010.

[5] He Qing, Duan Ye. Automatic detailed localization of facial features. Pattern Recognition Letters, under review.

Appendices

Automatic detailed localization of facial features

Qing He[1], Ye Duan
Department of Computer Science, University of Missouri, Columbia, MO, USA 65211
qhgb2@mizzou.edu, duanye@missouri.edu

Abstract
We propose a complete framework for automatic detailed facial feature localization, for the purpose of computer based syndrome classification. Particularly, we are interested in the features of the eyes, the nose and the mouth. Face detection is performed followed by the region detection that locates a rough bounding box of each facial component, and detailed features are then extracted within each bounding box. Since the feature points lie on the shape contours, we start from shape contour extraction, and then detect the feature points from the extracted contours. In the eye and nose feature detection, a local minimum map is constructed followed by curve detection and fitting. In the mouth feature detection, the lip is first segmented based on the color information and the lip contour is extracted by fitting parabola curves. Experimental results show the robustness and accuracy of our methods.

Keywords: facial feature localization, eyelid, nose boundary, lip contour, Hough transform

1 introduction

Automatic localization of facial features is important technique in many applications, such as face recognition, human-computer interaction, surveillance, etc. Particularly, computer aided diagnosis is becoming an attracting application in recent years. For example, the presence of a specific facial pattern in patients with a genetic syndrome indicates phenotypic expression of this disease, and the question has been asked whether a computer can recognize and classify dysmorphic faces solely on the basis of 2D images. Dalala and Phadk (2007), Loos et al. (2003), Boehringer et al. (2006) performed syndrome classification based on the feature points extracted from facial images, but the feature points were manually identified in their works. We aim at developing an automatic method to locate facial features for the purpose of computer based diagnosis, but the approach is applicable to other fields with similar requirement.

Various methods for facial feature detection/localization have been reported in literatures. Face detection is usually the first step in facial feature detection in order to provide a region for facial features to be detected. Feris et al. (2001) proposed a two-level Garbor wavelet network (GWN) to detect eight facial features. In Bhuiyan et al. (2003) six facial features are detected. Face detection is performed using skin color segmentation and genetic algorithm. Image enhancement is then performed and the facial features are detected through intensity threshold. In Gourier et al. (2004), an elliptic facial region is detected based on skin color. A vector of Gaussian derivatives and the linear combination of these descriptors act as detection functions for facial features. In Cristinacce et al. (2004), a multi-stage approach is used to locate 17 facial features. The face is detected using boosted cascaded classifier (Viola and Jones 2004), and the same classifier is trained using facial feature patches. Further refinement is achieved by active appearance model (Cootes et al. 2001). Asteriadis et al. (2009) detect eye centers and mouth corners using a hierarchical scheme. After face detection and normalization in size, a distance vector field (DVF) is created according to the distance from each pixel to the closest edge. The eye and mouth regions are found by matching the DVF with a template. Intensity and color information is then used to locate eye centers and mouth corners within the detected regions.

All the above works only look for feature points. However, more details of facial features lie in their shape information, such as eyelid and lip contours. While it may not be too tedious to label a few feature points manually, it is almost impractical to delineate shapes of facial features by hand. Therefore, an automatic procedure for facial feature shape extraction is in demand, which is the main focus of this paper.

Lip contour extraction has been a branch with extensive studies in the past decade. Since the lip is rich in color, most previous works utilized the color information to separate the lip form the background, and then some refined methods were used to extract the accurate lip contour. Wang et al. (2004) used three quadratic curves to characterize the lip contour, with 16 points on the curves as parameters. The lip region was first separated from the background using fuzzy C-means clustering with shape constraints (Wang et al. 2002). Eveno et al. (2004) used several cubic curves to model the lip contour. Feature points on the upper lip were first detected using “jumping snake” which is robust to the initialization. Hybrid edge (Eveno et al. 2002) was computed from pseudo-hue which intensifies the

[1] corresponding author: 1 5735294358

upper lip edge. Yokogawa et al. (2007) matched a template of four quadratic curves to the lip contour, and the lip was first separated from the background by thresholding the hue component. Active contour model was also used in several literatures. Wakasugi et al. (2004) proposed an edge detection method based on the separability of two color intensity distributions, which was used as the image energy in the active contour model. A level set method without re-initialization was proposed in Sohail and Bhattacharya (2007), where only grayscale images were used.

Much fewer studies exist for eyelid and nose contour extraction. Vezhnevets and Degtiareva (2003) proposed an eye contour extraction method. Iris was first detected based on its intensity and circular shape. The points on the upper eyelid were then detected by Hough transform. A cubic curve was used to fit the upper eyelid points and a quadratic curve was used to fit the lower eyelid. Zheng et al. (2005) used Gabor filter to detect the eye corners and the top and bottom points of the iris, which were then used as control points for a spline curve to fit each eyelid. Ding and Martinez (2008) performed complete facial feature detection including the shape of the eyes, nose, mouth, eyebrows and the lower chin. A classifier was trained for eye corners and mouth corners respectively. The eyelid points were then detected and fitted to a cubic curve in a way similar to Vezhnevets and Degtiareva (2003). The mouth and nose boundaries were detected using some simple thresholding and the gradient information. Earlier works (Kampmann and Zhang 1998; YUILLE et al. 1992) used edge based deformable models to fit the shape contours of facial features, but it has been stated in Vezhnevets and Degtiareva (2003) that the edge information is not robust due to spurious edges and discontinuous edges.

We propose a complete framework for automatic detailed facial feature localization (Fig.1). Features of the eyes, the nose and the mouth are of interest (Fig.2), and more explanations of these features will be shown later. Face detection is performed followed by the region detection that locates a rough bounding box of each facial component, and detailed features are then extracted within each bounding box. Generalized Hough transform is applied for both eyelid and nose boundary detection, and color information is used for a rough lip region segmentation following by a curve fitting. Most of the feature points can be detected from the boundary contours. Our method is different from the previous works in that 1) more points on the lower eyelid are detected before the final curve fitting, while previous works only used two or three points to fit the lower eyelid contour. 2) it is the first time to use Generalized Hough transform for the nose boundary detection, which is more robust than simple thresholding methods in previous works. 3) five parabola curves are used to model the lip contour, which have simpler and more flexible parameters to adapt to different shape.

The primary application of our work is computer based diagnosis, so a few assumptions are made on the input image. We assume the input is a frontal color face image with neutral expression. The face should take the majority of the image area, and should not be occluded by hair, beard, etc. There should be no in-plane rotation or out-of-the-plane rotation of the face. Usually these assumptions are easy to satisfy in clinical applications.

The reminder of this paper is organized as follows. Section 2 describes region detection by parametric template matching, section 3~5 describe the detailed methods for the feature extraction of the eyes, the mouth and the nose, section 6 shows the results and validation, and section 7 concludes the paper.

2 face detection and region detection

2.1 face detection

Prior to any feature detection, face detection is applied using the method in Nilsson et al. (2007). Briefly, the local Successive Mean Quantization Transform features are proposed for illumination and sensor insensitive operation in object recognition. A split up Sparse Network of Winnows is presented to speed up the original classifier, and the features and classifier are combined for the task of frontal face detection. The input image is first converted to grayscale for face detection and the subsequent feature detections, except that the color version is retained for mouth feature detection. The image is then cropped to the detected face area as shown in Fig.3(b), which covers all the facial components but not the entire face. To facilitate the following template matching, the cropped image is rescaled to a standard size, e.g., the size of the template face image.

2.2 parametric template matching

Template matching is the process of comparing a standard pattern (template) with an image for the purpose of finding the occurrence of the template pattern within the search image. The search is performed by moving the template pixel by pixel over the search image while calculating the correlation between the template and the portion of the search image at that position to find the position with the highest normalized correlation value. High computational cost has been a major difficulty of this method. However, if the search area is small this problem can be greatly alleviated. The parametric template (Tanaka et al. 2000) is a linear combination of a set of templates with different feature values (scales, rotations, etc). It has many advantages over traditional template matching in that it can represent geometrical and non-geometrical changes of an object in the parametric template space.

Here we briefly introduce the concept of parametric template. A root template t_0 is defined as the template directly obtained from a template image. A set of vertex templates can be generated from the root template by geometric or non-geometric transformation. Let $t_1,...t_M$ be M normalized vertex template with the same size, the parametric template is defined as:

$$t_w = (\sum_{i=0}^{M} w_i t_i) / \| \sum_{i=0}^{M} w_i t_i \| \quad (0 \le w_i \le 1, \sum_{i=0}^{M} w_i = 1) \quad (1)$$

When comparing the template and an image patch g (normalized) with the same size of the template, our goal is to maximize the normalized correlation $\rho(g, t_w)$ by varying the parameters $\vec{w}$ subject to the constraints in (1), which can be solved by Lagrange multiplier method. The solution is

$$\vec{w} = H^{-1}\vec{G} / (\vec{n}, H^{-1}\vec{G})$$

$$\vec{w} = \begin{bmatrix} w_0 \\ \vdots \\ w_M \end{bmatrix}, \; H = \begin{bmatrix} (t_0, t_0), \cdots, (t_0, t_M) \\ \vdots \quad \ddots \quad \vdots \\ (t_M, t_0), \cdots, (t_M, t_M) \end{bmatrix}, \; \vec{G} = \begin{bmatrix} (g, t_0) \\ \vdots \\ (g, t_M) \end{bmatrix}, \; \vec{n} = \begin{bmatrix} 1 \\ \vdots \\ 1 \end{bmatrix} \quad (2)$$

In order to satisfy the constraints of $\vec{w}$ in (1), normalization needs to be performed on $\vec{w}$ as follows.

$$\vec{w} = \vec{w} / (\sum_{i=0}^{M} w_i) \quad (3)$$

A feature value v_i is bound to each vertex template t_i. After the parameters $\vec{w}$ are obtained, the feature value v of the parametric template t_w can be calculated as

$$v = \sum_{i=0}^{M} w_i v_i \quad (4)$$

2.3 region detection

The parametric template method is applied to the region detection. Scale variation of the objects is the major concern. Although the face is normalized to a standard size, there is still variation in the size of each individual facial component among different people. We take into account the size variation in both x and y directions. Therefore, a feature vector $\vec{v}_i$ instead of a scalar is assigned to each vertex template, which consists of the scales in x and y directions relative to the root template.

The root template for each facial component is shown in Fig.3(c). Each template is constructed such that some margin is included but no part of other component is included. Five vertex templates are generated from each root template, which are scaled in x direction only, y direction only, and both x, y directions. In order to compute the linear combination of the templates according to (1), the root template and its derived templates are first aligned by their centers, and all the templates are padded to the size of the largest vertex template so that they have the same size. The resulting parametric template has the same size as the largest vertex template.

In the search process, we utilize the prior knowledge about the approximate positions of facial components. Thus, we search for the eyes only in the upper half of the face area, and the right eye and the left eye are searched within the right and left half of the region respectively. The mouth is searched only in the lower half of the face. After the eyes and the mouth are detected, the nose is searched within the region below the eyes and above the mouth.

With the regions detected, the feature localization will be performed on the image patch of each specific region. For the eyes and the nose, the region image patches are cropped from the grayscale image, and for the mouth the region image patch is cropped from the color image.

3 eye feature extraction

3.1 overview

We are interested in four feature points shown in Fig.2(a) as well as the eyelid contours. En (endocanthion) is the point at the inner commissure of the eye fissure, ex (ectocanthion) is the point at the outer commissure of the eye fissure, pi (palpebrale inferius) is the lowest point in the mid-portion of the free margin of the lower eyelid, and ps (palpebrale superius) is the highest point in the mid-portion of the free margin of the upper eyelid. These four points are usually of most interest to clinicians. In the following we describe the method for the right eye, and for the other eye we mirror the eye image first before the feature detection.

3.2 iris detection

The eye image is first smoothed by a Gaussian filter and normalized in intensity. The reflection in iris is then removed using the method in Asteriadis et al. (2009). Briefly, a binary image is generated using otsu's histogram algorithm (Otsu 1979), and any white spot whose area is smaller than 20 pixels is filled with black (Fig.4(d)). After that, the corresponding pixels in the original image are filled with the intensity of their surrounding pixels (Fig.4(f)).
Template matching method described in 2.1 is then used to locate the iris on the binary image, and the root template is a binary image of the iris. The detected iris region is shown in Fig.4(e). The top and bottom boundaries are extracted from the detected iris binary image. The top boundary will serve as part of the upper eyelid contour, which will be discussed in the next section. Two key points are located on the bottom boundary, which are the corners of the iris and the sclera (Fig.4(f)). They can be found by searching for the first curvature extrema from each side of the bottom boundary.

3.3 eyelid extraction

The eyelid model consists of an upper eyelid curve and a lower eyelid curve, connecting at corner points en and ex. As stated in Vezhnevets and Degtiareva (2003), edge map does not give a robust estimation of the eyelids, and luminance valley points along the horizontal lines were detected as the candidate upper eyelid points. Our method is mostly inspired by Vezhnevets and Degtiareva (2003). To detect the upper eyelid, a local minimum map is constructed where each local minimum point is the luminance valley point in either horizontal or vertical direction (Fig.5(a)). Since the middle part of the eyelid contour is already detected in 3.2, we only look for the upper eyelid points to the two sides of the iris. As shown in Fig.5(a), these two parts of the upper eyelid are well captured by the local minimum map, and two straight lines can approximately fit the local minimum points on these two parts. We apply Hough transform (Duda and Hart 1972) to detect the two straight lines from the local minimum map. Hough transform is known to be robust to imperfect data and noise. In order to reduce the search space, we restrict the locations of lines based on the iris detection result in 3.2. Particularly, the two key points in Fig.4(f) serve as the left and right bound for the right and left parts respectively, and a horizontal line passing the topmost point of the middle upper eyelid serves as the upper bound (Fig.5(b)). Hough transform produces a set of lines within each search range, and the line with maximum number of local minimum points is selected. The points on the selected lines are the candidate eyelid points (Fig.5(c)).
Some false positive points that exceed the bound of the eye may be included in the detected lines. A corner localization procedure is applied to locate the eye corners from the candidate eyelid points. Only the eyelid points that are in between the two eye corners are retained, and others are discarded (Fig.5(d)). The template matching method in 2.1 is again applied for eye corner detection. The root templates here are the 9x9 patches centered at the left and right eye corners respectively. Instead of searching the entire eye image, we only go through the locations of each candidate eyelid point, and the point location at which there is a best match with the template is selected as the corner position.
The retained points on the two sides of the upper eyelid together with the points on the middle eyelid curve detected in 3.2 constitute the upper eyelid points. A Bezier curve is fitted to all these points to obtain the upper eyelid contour (Fig.5(e)). Since the Bezier curve interpolates the end points, the resulting eyelid contour always pass through the two eye corner points.
Fig.5(a) shows that the local minimum map does not capture the lower eyelid very well, because the contrast on the lower eyelid is not as strong. In Vezhnevets and Degtiareva (2003) and Zheng et al. (2005), a quadratic curve is fitted to the eye corners and the lowest point of the iris to generate the lower eyelid. However, this curve may not approximate the lower eyelid very well because a major portion of the lower eyelid in between the three points is missing. We approximate the lower eyelid by a piecewise linear curve which consists of four line segments. They are divided by the following five points: two eye corners (A,E), left lower bound of the iris (B), right lower bound of the iris (D), the lowest point in the middle of the iris (C) (Fig.6(a)). The two eye corners have been detected before so they are fixed, but the other three points are flexible to move. We start from the line segment connecting the left corner (A) and the left lower bound of the iris (B). By moving point B along vertical direction within a small range we can form several candidate lines. On each line the average gradient magnitude is calculated and the line with the maximum gradient magnitude is selected. The same method is used for the line segment between the right corner (E) and the right lower bound of the iris (D). Then we form several polyline candidates connecting the lower left (B), low middle (C), and lower right bound (D) of the iris, by moving the low middle point of the iris along the vertical direction. The polyline with maximum average gradient is selected. Fig.6(b) shows the points on the selected line segments for the lower eyelid.

A Bezier curve is fitted to all the points on the above line segments to obtain the lower eyelid contour (Fig.6 (c)). The same as the upper eyelid contour, the lower eyelid contour also pass the two eye corner points. Therefore, the upper and lower eyelid contours connected by the same end points form an entire eye boundary (Fig.6(d)).
With the upper and lower eyelid contour, The feature points in Fig.2(a) are easy to obtain. En and ex are already detected which are the two eye corners. pi and ps are the lowest and highest points on the eye boundary (Fig.6(d)).

4 lip contour extraction

4.1 overview

Six feature points (Fig.2(b)) are of interest as well as the lip contour. Ch's (cheilion) are the mouth corners, li (labiale inferius) is the middle point of the lower lip, lss's are the highest points on each side of the upper lip, and ls (labiale superius) is the lowest point in between the two lss's. These points are not only defined from clinical point of view, but also serve as parameters for the curve fitting which will be shown later.

4.2 region based lip segmentation

The mouth is rich in color so color images are often used for mouth feature detection. Various color spaces (HSV, Lab, Luv, RGB) have been explored (e.g.,Wang et al. 2004; Eveno et al. 2004; Yokogawa et al. 2007). A fuzzy C-means (FCM) method incorporating shape information (Wang et al. 2002) has been proposed to cluster the lip region based on selected color components. This method assumes an ellipse shape of the mouth and can better eliminate noisy regions produced from FCM. However, when the mouth is long and thin the ellipse model cannot approximate it very well. A new color transformation Eveno et al. (2001) represents each pixel as the curvature of a parabola defined by three points in the transformed color space. Generally this method can generate regions close to the mouth shape, but a threshold needs to be selected manually for different images.
We apply a method similar to Lievin et al. (1999) which is much simpler than the above two methods. The ratio image R/G is computed, and then the pixel values of the resulting image are truncated to within 2.5 standard deviations around the mean pixel value. This can effectively remove the few extremely high ratios due to image noise. The histogram of this ratio image will have two peaks, the higher one being the skin and the lower one being the lip. Otsu's method is applied again to find the optimal threshold on this ratio image. A binary image is then generated based on this threshold (Fig.7(b)). Connected components algorithm (Dillencourt et al. 1992) is performed to remove small background noise and holes in the mouth region. Then the boundary of the mouth is extracted to get an initial contour (Fig.7(c)).

4.3 parabola model for the lip contour

We use parabolas to model the lip contour. Four parabolic curves (yl, ylr, yrl, yr) are used to approximate the upper lip and one (yb) to approximate the lower lip (Fig.8). The intersection points of the upper lip curves are $\vec{p}_1$, $\vec{p}_2$ and $\vec{p}_3$, where $\vec{p}_1$ and $\vec{p}_3$ are also the zero-derivative points of the connecting parabolas. $\vec{p}_4$ is the zero-derivative point of curve yb. The reason to use four parabolas instead of two for the upper lip is that the curve between $\vec{p}_1$ and $\vec{p}_3$ may not follow the same parametric form as the curve on the other side of $\vec{p}_1$ and $\vec{p}_3$. Moreover, bending and expansion are applied to the point (x, y) on the curve as follows.

$$x' = T(B(x, y), y) \qquad (5)$$

where x' is the new x coordinate of point (x, y) and the y coordinate does not change. $B(x, y)$ is the bending function (Wo¨ rz and Rohr 2006) and $T(x, y)$ is the expansion function defined as follows:

$$B(x, y) = x - y^2\delta \ , \ T(x, y) = (x - x_0) / \exp(y \cdot s) + x_0 \qquad (6)$$

where x_0 is the x coordinate of the zero-derivative point of the parabola and δ, s are coefficients. The sign of s determines the shrinking or expansion of the curve along x direction.
The origin of the coordinate system is at the left mouth corner, and the x,y axes are shown in Fig.8. The coefficients of each parabola curve can be derived from points $\vec{p}_1 \sim \vec{p}_4$ as well as the two mouth corner points $\vec{p}_l$ and $\vec{p}_r$. The parameters to be optimized are the coordinates of these six control points and the coefficients for expansion and bending of each curve.
The optimization is performed by maximizing an energy function. The energy function in (Wang et al. 2004) is based on pure region information obtained from clustering. If there are some misclassified pixels in the probability

map, the fitted curve will likely copy this error. We use an energy function as follows which combines region and gradient information.

$$E = \int_C grad(\vec{p})d\vec{p} + \alpha \int_C region(\vec{p})d\vec{p} \ , \quad region(\vec{p}) = \frac{1}{2}\sum_k \frac{(h(k,\Omega_{ip}) - h(k,\Omega_{op}))^2}{(h(k,\Omega_{ip}) + h(k,\Omega_{op}))^2} \qquad (7)$$

where $grad(\vec{p})$ is the normalized gradient magnitude at point $\vec{p}$, *h(k,I)* is the kth histogram bin value of image I, Ω_{ip} and Ω_{op} are the regions inside and outside the mouth in a small neighborhood of point $\vec{p}$, and *C* includes the entire lip contour. $region(\vec{p})$ defines the region difference in the neighborhood of each point. α is the coefficient to balance the two terms.

4.4 parameter initialization and optimization

The rough positions of the control points can be estimated from the initial mouth contour obtained in 4.2. First, the leftmost and rightmost points are identified as mouth corners. After the two corner points are located, we detect the rough locations of other four control points from the initial contour. The coordinate system in Fig.8 is first constructed, with the line connecting the two corner points as the x axis. Under this coordinate system, the middle point in the x direction on the upper lip is first located, and the point in the vicinity of this point with the highest y coordinate is $\vec{p}_2$ (note that y axis is pointing down). $\vec{p}_2$ divides the upper lip into left and right parts. On each part the point with smallest y coordinate is $\vec{p}_1$ and $\vec{p}_3$ respectively. On the lower lip contour the middle point in the x direction is $\vec{p}_4$. Fig.9(a) shows the estimated initial positions of the control points.

Other parameters to be optimized are the bending parameter δ and the expansion parameter s for each parabola curve. We set $s = 0$ and $\delta = 0.0001$ for each curve. The optimization is constrained by the following inequalities to ensure reasonable spatial relation among $\vec{p}_1(x_1, y_1)$, $\vec{p}_2(x_2, y_2)$ and $\vec{p}_3(x_3, y_3)$.

$$x_1 < x_2 < x_3, y_2 > y_1, y_2 > y_3 \qquad (8)$$

Moreover, the mouth corners are constrained on the minimum luminance line, so only the *x* coordinates of the moth corners need to be optimized.

The feature points in Fig.2(b) coincide with the control points in Fig.8, so the optimized parameters of the parabola curves give the coordinates of the feature points as well. Fig.9(b) shows the lip contour and the feature points after optimization.

5 nose boundary extraction

5.1 overview

Very few literatures have reported feature detection on the nose, probably because the nose does not have distinct feature points as the mouth and the eyes do. In this paper, we are interested in the alare point which is the most lateral point on each side of the nose (Fig.2(c)), and the nose boundary passing through the alare point on each side. However, since each boundary is an open contour, there is no clear upper or lower bound of the contour.

5.2 nostril detection

In order to facilitate the detection of the nose boundary, we first locate the rough positions of the nostrils. The average intensities of the rows and the columns of the image are calculated, generating a horizontal profile and a vertical profile of the intensity (Fig.10(a)). The x coordinates of the nostrils can be found at the local minima on the horizontal profile, and the y coordinate can be found at the local minimum on the vertical profile The search range of the nose boundaries is then limited to the two sides of the nostril points (Fig.10(b)).

5.3 nose boundary detection

Since the nose boundary is usually weak, histogram equalization is first applied on the grayscale nose image to enhance the contrast (Fig.11(a)). An edge map of this enhanced nose image can usually capture most of the nose boundaries. However, it is not always possible to get perfect edges around the nose boundaries, and an example of the missing edge around one boundary is shown in Fig.11(b). Alternatively, local minimum map (Fig.11(c)) can be applied here as well which is very close to the edge map around the boundary points, but similar problems may occur as with the edge map. Therefore, we decide to fuse the edge map and local minimum map into a combined map that can capture the boundary points more robustly. Specifically, a local minimum point is added to the edge

map only if there is no surrounding edge point in a small neighborhood of this local minimum point. Then the edge/local minimum points (or pixels) are grouped by connected components algorithm, and small components are discarded. Fig.11(d) shows the combined map from Fig.11(b) and (c) after small components removal, where the missing edge is filled in by local minimum points.

Generalized Hough transform for arbitrary shapes is then used to detect the boundary contours from the combined map. A template shape and a reference point need to be defined first, and a lookup table is constructed recording the location of each point on the template shape relative to the reference point. Given the location of the reference point, a shape can be generated from the lookup table, thus each point in the Hough space (i.e., reference point) corresponds to a shape in the image space. Assuming that the rotation and scaling of the shape do not change, we have the coordinates of the reference point as the only parameters. Since these parameters are equivalent to those in the line detection with Hough transform, the algorithm for the curve detection follows the same routine as the line detection. In our implementation, the template for each nose boundary is a generic shape of the nose boundary, and the reference point is chosen as the leftmost (rightmost) point for the left (right) boundary (Fig.11(e)). With the results of the nostril locations, the range of the parameters is restricted to the part of the image shown in Fig.10(b). Rotation and scaling parameters can also be included, but the computational cost will be significantly increased. We find that a fixed template shape can serve our purpose as well since the nose boundaries do not vary too much among different individuals, so we do not consider rotation and scaling parameters.

A Bezier curve is then used to fit the detected local minimum points on each boundary. The alare points are then located by finding the left most and rightmost point on each contour respectively (Fig.11(f)).

6 results and validation

The proposed method is tested on FERET database (Phillips et al. 1998; Phillips et al. 2000), which contains various color images of faces with different expressions, rotations and lighting conditions. From the frontal face subset, the images that obviously violate our assumptions are removed, and 100 images are randomly selected from the remaining images which meet our assumptions to a maximum extent. Slight facial expressions and head rotations are tolerable for our method. Each image has the dimension of 512*768 pixels and includes the full head and the neck of a single person against a near-white background (Fig.3(a)). Fig.12 shows several results on the detected face images, from which we can see the extracted feature points and boundary contours are faithful to the image data.

In order to quantitatively evaluate the performance of our method, the feature points are manually labeled on each image by three different operators. The ground truth position (P) is taken as the average of the manually labeled positions from the three operators. For each feature point on an individual image, the accuracy of our detection result is calculated as

$$a = 1 - \| \vec{p}_g - \vec{p}_t \| / d_w \quad (9)$$

where $\vec{p}_g$ is the ground truth position of this feature point, $\vec{p}_t$ is the position obtained by our method, $\|.\|$ is the Euclidean distance, and d_w is the width of the corresponding facial component. For example, d_w is the eye width when the accuracy of an eye feature point is calculated, which can be estimated from the distance between the ground truth positions of two eye corners. The value of a is truncated to [0,1]. The result of a feature point is considered successful if its accuracy is above a threshold T, and the result of an entire image is successful if all the feature points are successfully detected. The overall success rate for each feature point is the percentage of the successful cases, and the overall success rate for all feature points is the percentage of successful images.

Among all the results, there is no failure in face detection or region detection. Note that the face detection is considered successful if all the facial components of interest are completely inside the detected face, and the region detection is considered successful if all the related feature points are inside the detected region. Among all the failure cases, the main cause of the mouth failure is the incorrect separation between the lip and the skin due to the lack of color constancy under poor lighting. The failure on the eye features is mostly because the iris is connected to other parts in the binary image thus leading to incorrect iris detection. The failure of the nose features is mainly due to extremely low contrast on that particular boundary. Table 1 shows the average accuracy of each feature point, the success rate for each feature point and the overall success rate. The success rate of individual feature point remains high even with a high threshold T, although the overall success rate declines faster with the increasing T because it is affected by every single feature point.

No validation of the boundary contours is performed because it is difficult to provide the ground truth by manually delineating the contour. Since most of the feature points are obtained from the contours, the accuracy of the feature point detection can reflect the accuracy of the boundary extraction to some extent.

7 conclusion

This paper proposes a framework for automatic facial feature detection. Features of the eyes, the nose and the mouth are extracted. To our knowledge this is the first work to extract a complete set of major facial feature points and boundary contours. The primary application of this work is the computer aided diagnosis, so only frontal images are considered and some other assumptions of the input image are made. Visual inspection of the experimental results shows the accuracy of the overall feature detection, and quantitative validation further demonstrates the accuracy of the feature point detection.

Acknowledgement

Portions of the research in this paper use the FERET database of facial images collected under the FERET program, sponsored by the DOD Counterdrug Technology Development Program Office. This work is supported in part by an NIH pre-doctoral training grant for Clinical Biodetectives, a Thompson Center Research Scholar fund, the Department of Defense Autism Concept Award, and the NARSAD Foundation Young Investigator Award.Thanks Dmitriy Karpman, Chao Fang and Shiyuan Chen for the help of the validation experiemnt.

References

Asteriadis, S., Nikolaidis, N., Pitas, I., 2009. Facial feature detection using distance vector fields. Pattern Recognition 42, 1388 – 1398

Boehringer, S., Vollmar, T., Tasse, C., Wurtz, RP., Gillessen-Kaesbach, G., Horsthemke, B., Wieczorek, D., 2006. Syndrome identification based on 2D analysis software. Eur J Hum Genet. 14(10), 1082-9.

Dalal, AB., Phadk, SR., 2007. Morphometric analysis of face in dysmorphology. Computer Methods and Programs in Biomedicine, 85(2), 165-172

Cristinacce, D., Cootes, T., 2003. Facial feature detection using AdaBoost with Shape Constraints. BMVC03, 231—240

Bhuiyan, MA., Ampornaramveth, V., Muto, S., Ueno, H., 2003. Face detection and facial feature localization for human–machine interface. National Institute of Informatics Journal, 5 (3), 25–39.

Cootes, T., Taylor, CJ., Cooper, DH., 1995. Active Shape Models - Their Training and Application, Computer Vision and Image Understanding, 61(1), 38-59

Cootes, T., Edwards, GJ., Taylor, CJ., 2001. Active appearance models. IEEE TPAMI, 23(6),681–685

Cristinacce, D., Cootes, T., Scott, I., 2004. A Multi-Stage Approach to Facial Feature Detection. BMVC04, 231—240

Dillencourt, MB., Samet, H., Tamminen, M., 1992. A general approach to connected-component labeling for arbitrary image representations. Journal of the ACM, 39(2), 253 - 280

Ding, L., Martinez, A., 2008. Precise detailed detection of faces and facial features. Proceedings of IEEE Conference on Computer Vision and Pattern Recognition.

DUDA, R., HART, P., 1972. Use of the hough transform to detect lines and curves in pictures. Communication of the Association of Computer Machinery 15(1), 11–15.

Eveno, N., Caplier, A., Coulon, PY., 2001. A New color transformation for lips segmentation. Proceedings of IEEE Fourth Workshop on Multimedia Signal Processing, 3–8.

Eveno, N., Caplier, A., Coulon, PY., 2002. Key Points Based Segmentation of Lips, Proc. ICME'02

Eveno, N.; Caplier, A.; Coulon, PY., 2004. Accurate and quasi-automatic lip tracking. IEEE Transactions on Circuits and Systems for Video Technology,14(5), 706- 715

Feris, RS., Gemmell, J., Toyama, K., Krüger, V., 2001. Hierarchical Wavelet Networks for Facial Feature Localization. ICCV'01 Workshop on Recognition, Analysis and Tracking of Faces and Gestures in Real-Time Systems

Gourier, N., Hall, D., Crowley, JL., 2004. Facial features detection robust to pose, illumination and identity, International Conference on Systems Man and Cybernetics, 617–622.

Jahanbin, S., Choi, H., Jahanbin, R., Bovik, AC., 2008. AUTOMATED FACIAL FEATURE DETECTION AND FACE RECOGNITION USING GABOR FEATURES ON RANGE AND PORTRAIT IMAGES. Proceedings of the International Conference on Image Processing,

Kampmann, M., Zhang, L., 1998. Estimation of eye, eyebrow and nose features in videophone sequences. Int. Workshop on Very Low Bitrate Video Coding, 101–104

Lievin, M., Delmas, P., Coulon, PY., Luthon, F., Fristol, V., 1999. Automatic lip tracking: Bayesian segmentation and active contours in a cooperative scheme. IEEE International Conference on Multimedia Computing and Systems, 1, 691-696

Lina, YH., Chenb, CH., 2008. Template matching using the parametric template vector with translation, rotation and scale invariance. Pattern Recognition 41, 2413 – 2421
Loos, HS., Wieczorek, D., Würtz, RP., Malsburg, C., Horsthemke, B., 2003. Computer-based recognition of dysmorphic faces. Eur J Hum Genet. 11(8), 555-60
Nilsson, M., Nordberg, J., Claesson, I., 2007. Face Detection using Local SMQT Features and Split Up SNoW Classifier. IEEE International Conference on Acoustics, Speech, and Signal Processing
Otsu, N., 1979. A threshold selection method from gray-level histograms. IEEE Trans. Sys., Man., Cyber. **9**, 62–66
Phillips, P.J., Wechsler, H., Huang, J., Rauss, P., 1998. The FERET database and evaluation procedure for face recognition algorithms. Image and Vision Computing J, 16(5), 295-306
Phillips, P.J., Moon,H., Rizvi, SA., Rauss, PJ., 2000. The FERET Evaluation Methodology for Face Recognition Algorithms, IEEE Trans. Pattern Analysis and Machine Intelligence, 22, 1090-1104
Sohail, A., Bhattacharya, P., 2007. Automated Lip Contour Detection Using the Level Set Segmentation Method. 14th International Conference on Image Analysis and Processing
Tang, F., Tao, H., 2007. Fast multi-scale template matching using binary features. WACV 07
Viola, P., Jones, M., 2004. Robust real-time face detection, International Journal of Computer Vision 57 (2),137–154.
Tanaka, K., Sano, M., Ohara, S., Okudaira, M., 2000. A parametric template method and its application to robust matching. IEEE Conference on Computer Vision and Pattern Recognition, 1, 620–627.
Vezhnevets, V., Degtiareva, A., 2003. Robust and Accurate Eye Contour Extraction. Proc. Graphicon-2003, 81-84
Wakasugi, T., Nishiura, M., Fukui, K., 2004. Robust lip contour extraction using separability of multi-dimensional distributions. Proc. 6thIEEE Int. Conf. Automatic Face and Gesture Recognition, 415–420.
Wang, SL., Leung, SH., Lau, WH., 2002. Lip segmentation by fuzzy clustering incorporating with shape function. Proceedings of IEEE International Conference on Acoustics, Speech and Signal Processing, 1, 1077–1080.
Wang, SL., Laua, W.H., Leung, S.H., 2004. Automatic lip contour extraction from color images, Pattern Recognition 37, 2375 – 2387
Wo¨ rz, S., Rohr, K., 2006. Localization of anatomical point landmarks in 3D medical images by fitting 3D parametric intensity models. Medical Image Analysis, 10, 41–58
Yokogawa Y., Funabiki, N., Higashino, T., Oda, M., Mori, Y., 2007. A Proposal of Improved Lip Contour Extraction Method Using Deformable Template Matching and Its Application to Dental Treatment. Systems and Computers in Japan, 38(5)
YUILLE, A., HALLINAN, P., COHEN, D., 1992. Feature extraction from faces using deformable templates. International Journal of ComputerVision 8, 2, 99–111.
Zheng, Z., Yang, J., Yang, L., 2005. A robust method for eye features extraction on color image, Pattern Recognition Letters, 26, 2252–2261

Figure legends:
Fig.1 framework of the facial feature detection
Fig.2 feature points and boundary contours of the (a) eye (b) mouth (c) nose
Fig.3 (a) the input color image (b) the image converted to grayscale and cropped to the detected face (c) template of each facial component
Fig.4 (a) the original eye image (b) the result of Gaussian smoothing and intensity normalization of (a) (c) the binary image of (b) (d) the binary image after hole filling (e) the detected iris region (f) boundaries and key points extracted from the iris region, shown on the eye image after reflection removal
Fig.5 (a) local minimum points overlaid on the eye image (b) search range of the upper eyelid points (the lower left and lower right rectangle regions) (c) detected upper eyelid points by Hough transform (d) the entire set of upper eyelid points after eye corner detection (e) final upper eyelid contour
Fig.6 (a) piecewise linear curve of the lower eyelid (b) detected lower eyelid points (c) final lower eyelid contour (d) the entire eyelid boundary and the feature points
Fig.7 (a) the original mouth image (b) the binary image (c) the mouth contour extracted from (b)
Fig.8. pl, pr: mouth corner points; p1~p4: four points used to determine the parameters of the parabolas; y*: parabolas for different segments of the lip
Fig.9 (a) initial lip contour and the minimum luminance line (green line) (b) initial control points (c) final lip boundary and feature points
Fig.10 (a) illustration of the nostril detection (b) detected nostrils and the search range of the nose boundaries (rectangle regions on the left and right sides)

Fig.11 (a) nose image after histogram equalization (b) edge map of (a) (c) local minimum map of (a) (d) combined map after small components removal (e) template nose boundaries and the reference points (f) detected nose boundaries and feature points shown on the original nose image
Fig.12 detected feature points and contours on several color images

Figures:

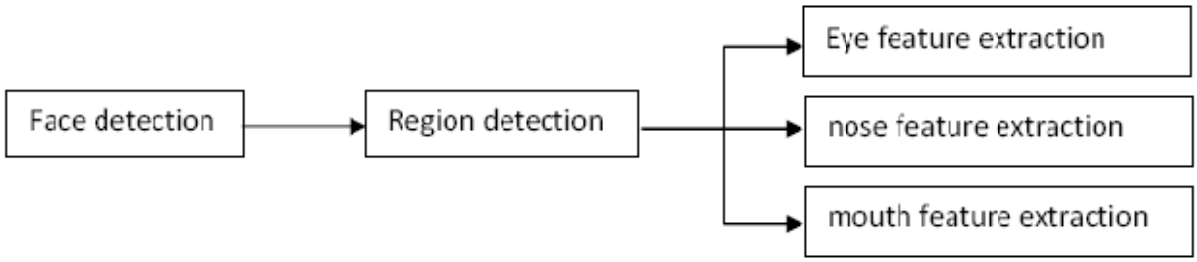

Fig.1

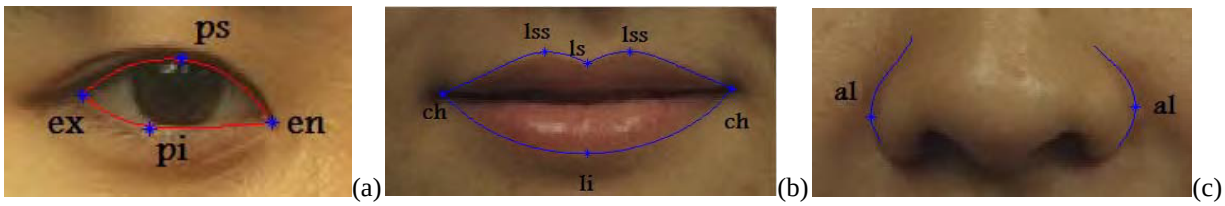

Fig.2

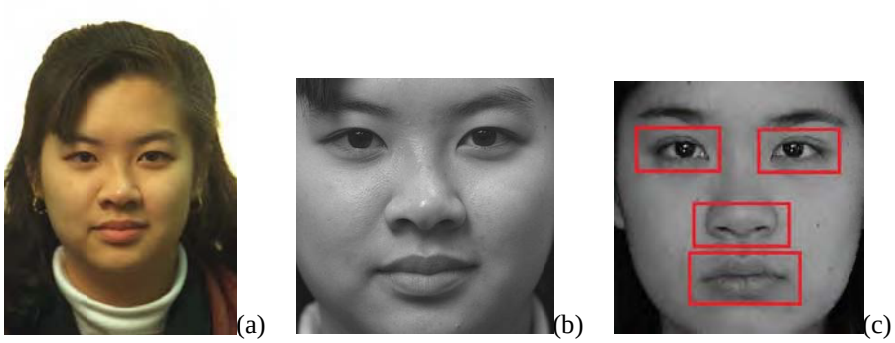

Fig.3

Fig.4

Fig.5

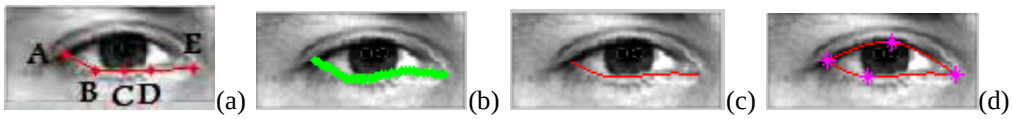

Fig.6

Fig.7

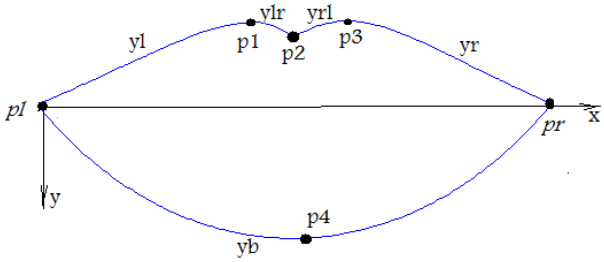

Fig.8.

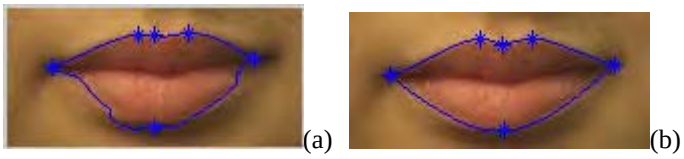

Fig.9

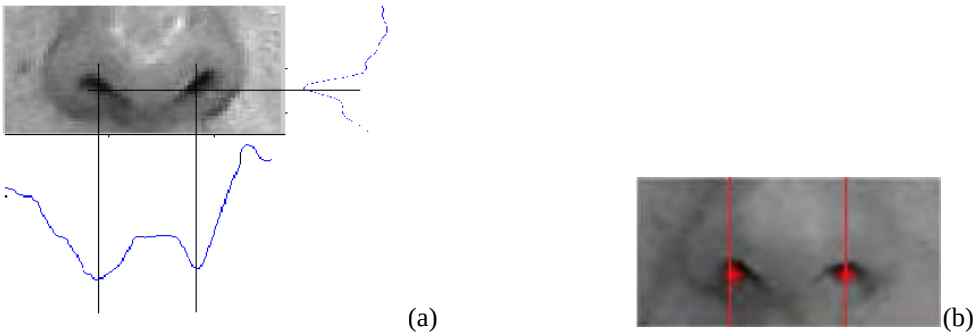

Fig.10

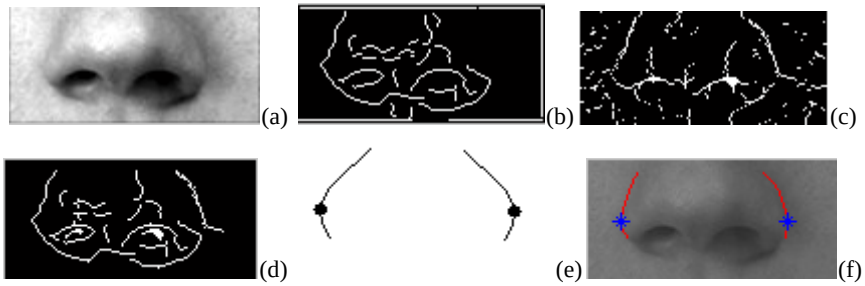

Fig.11

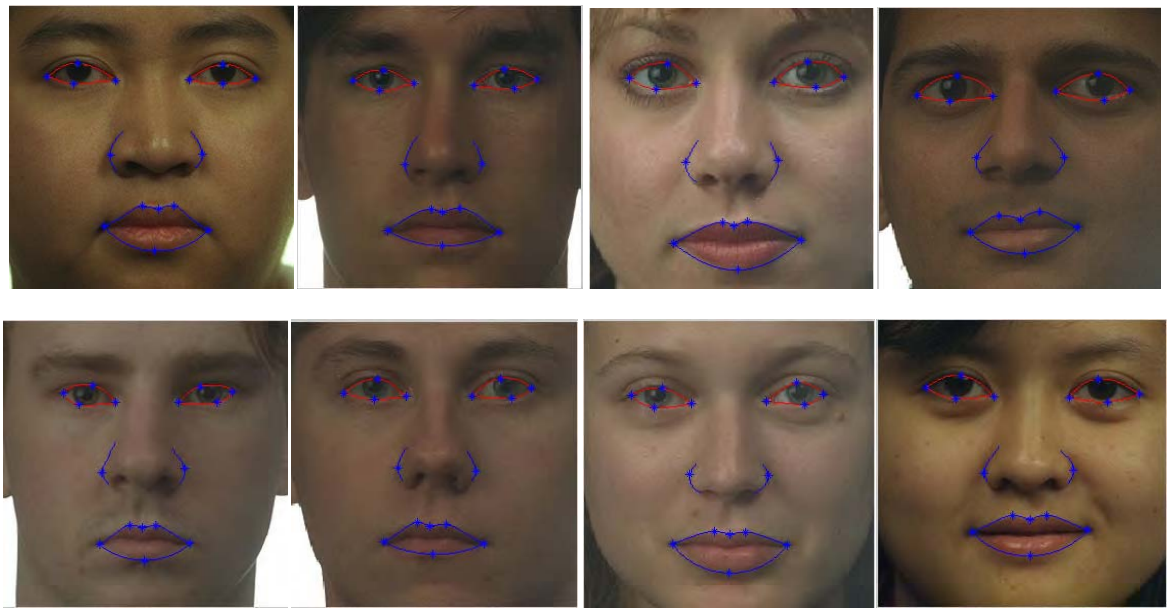

Fig.12

Table 1 success rate of each feature point and the overall success rate

Facial components	**Feature points**	**Accuracy**	**Success rate**	
			T=0.95	**T=0.9**
Left eye	ex	0.952	0.68	1
	en	0.943	0.63	1
	ps	0.919	0.61	0.75
	pi	0.945	0.72	0.89
Right eye	en	0.941	0.62	1
	ex	0.938	0.68	1
	ps	0.912	0.68	0.77
	pi	0.948	0.70	0.91
Nose	Al (left)	0.903	0.58	0.63
	Al (right)	0.938	0.75	0.89
mouth	Ch (left)	0.993	1	1
	Lss (left)	0.988	0.99	0.99
	Ls	0.988	0.99	0.99
	Lss (right)	0.984	0.99	0.99
	Ch (right)	0.963	0.84	0.95
	Li	0.959	0.88	0.96
Overall			0.52	0.90

Statistical 3D Shape Analysis of Lateral Ventricles in Autism

Qing He[a], Ye Duan [a, b], Judith Miles[b]

[a] Department of Computer Science, University of Missouri-Columbia, Columbia, MO, 65211, USA
[b] Thompson Center for Autism, University of Missouri-Columbia, Columbia, MO, 65211, USA
qhgb2@mizzou.edu, duanye@missouri.edu, MilesJH@health.missouri.edu

Introduction

Autism is a heterogeneous neurodevelopmental disorder of unknown etiology marked by social, emotional and communication impairments. The ventricular system is a structure in the center of the brain filled with fluid. Enlargement of the ventricles in autism has been reported in previous works. However, the magnitude of the differences revealed by volume analysis is limited, because it does not consider how shapes overlap each other. Shape analysis can precisely locate morphological changes in brain structures which cannot be reflected in volume measurements, thus it becomes more and more popular in neuroimaging community. Very few studies have been done with regard to the shape morphology of the ventricles in autism.

The aim of this paper is to study the shape differences of the lateral ventricles between autistic children and normal controls. 3D models of ventricle shapes are compared to reveal the shape difference at every surface location.

Participants

Five Children with autism were recruited from the Thompson Center for Autism and Neurodevelopmental Disorders. Four control subjects with matching gender, age and ancestry were recruited from the community. Student t-test was used to compare the ages and $\chi 2$ test was used to compare the gender ratios. There was no significant difference between the two groups in terms of age, gender and race. This study was approved by the Health Sciences Institutional Review Board. The parents or legal guardians of all subjects provided written consent for participation in this study.

Methods

The 3D ventricle models were obtained using the semiautomatic segmentation software that has been developed in our previous work. Six anatomical landmarks were identified. Pseudo-landmarks on the surface were then interpolated using the method in our previous work. Generalized Procrustes Analysis is performed on all the 3D shapes in order to eliminate the shape differences caused by translation, rotation and scaling. difference between groups at every surface location was tested using Hotelling T2 two-sample metric. Since comparisons are made at thousands of surface points, we adopted False Discovery Rate estimation (FDR) for p-value correction.

Results

From the overlaid average structures of the two groups (Fig.1(a)), we find that the posterior horns of both ventricles in autistic children are bent more inward, and the anterior horns are bent more downward in the autistic children. The amount of difference can be seen from the signed distance map (Fig.1(b)). A two-tailed alpha level of 0.05 is chosen as the significance threshold for the raw p-values. The raw significance maps of both ventricles show significant shape difference in part of the body and the posterior horns between autistic children and controls (Fig.1(c)), but the corrected significance maps show no shape difference between the two ˘rou¸ s (not shown).

Conclusion

This paper studies the shape differences of the lateral ventricles between autistic children and controls. The overlaid mean structures show shape difference in the anterior and posterior horns, but sstatistical tests do not show any significance in those differences. This may be due to small sample size and further experiment needs to be done when more data are available.

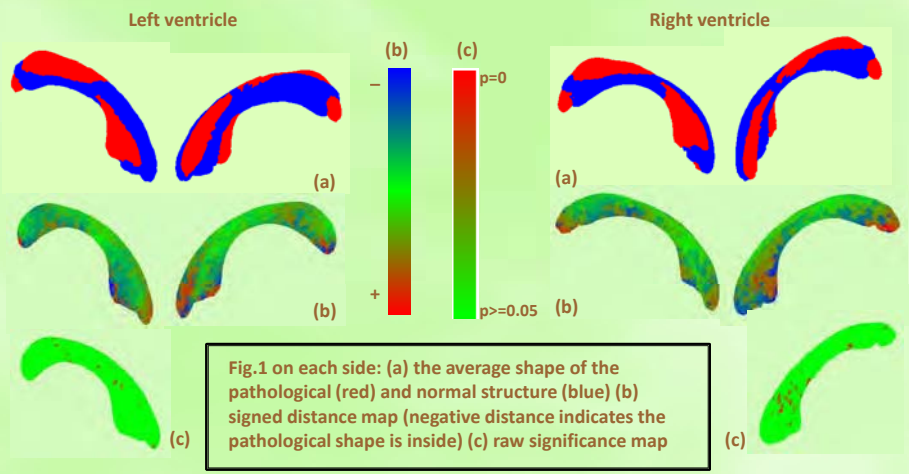

Fig.1 on each side: (a) the average shape of the pathological (red) and normal structure (blue) (b) signed distance map (negative distance indicates the pathological shape is inside) (c) raw significance map

Acknowledgements

This work is supported in part by the Department of Defense Autism Concept Award, and the NARSAD Foundation Young Investigator Award, and a NIH pre-doctoral training grant for Clinical Biodetectives.

COMMUNICATIONS IN NUMERICAL METHODS IN ENGINEERING
Commun. Numer. Meth. Engng (2009)
Published online in Wiley InterScience (www.interscience.wiley.com). DOI: 10.1002/cnm.1250

Detecting corpus callosum abnormalities in autism subtype using planar conformal mapping

Ye Duan[1], Qing He[1,*,†], Xiaotian Yin[2], Xianfeng Gu[2], Kevin Karsch[1] and Judith Miles[3]

[1]*Department of Computer Science, University of Missouri-Columbia, Columbia, MO 65211, U.S.A.*
[2]*State University of New York at Stony Brook, Stony Brook, NY 11794, U.S.A.*
[3]*Thompson Center for Autism, University of Missouri-Columbia, Columbia, MO 65211, U.S.A.*

SUMMARY

A number of studies have documented that autism has a neurobiological basis, but the anatomical extent of these neurobiological abnormalities is largely unknown. In this paper, we apply advanced computational techniques to extract 3D models of the corpus callosum (CC) and subsequently analyze local shape variations in a homogeneous group of autistic children. Besides the traditional volumetric analysis, we explore additional phenotypic traits based on the oriented bounding rectangle of the CC. In shape analysis, a new conformal parameterization is applied in our shape analysis work, which maps the surface onto a planar domain. Surface matching among different individual meshes is achieved by aligning the planar domains of individual meshes. Shape differences of the CC between autistic patients and the controls are computed using Hotelling T^2 two-sample metric followed by a permutation test. The raw and corrected p-values are shown in the results. Additional visualization of the group difference is provided via mean difference map. Copyright © 2009 John Wiley & Sons, Ltd.

Received 7 February 2008; Revised 24 April 2008; Accepted 19 February 2009

KEY WORDS: corpus callosum; autism; shape analysis; planar conformal mapping; permutation test; phenotypic traits

1. INTRODUCTION

A number of studies have documented that autism has a neurobiological basis, but the anatomical extent of these neurobiological abnormalities is largely unknown [1]. Several studies have reported deficits in the size of the corpus callosum (CC) and its sub-regions, although the results are

*Correspondence to: Qing He, Department of Computer Science, University of Missouri-Columbia, Columbia, MO 65211, U.S.A.
†E-mail: qhgb2@mizzou.edu

Contract/grant sponsor: Thompson Center for Autism and Neurodevelopmental Disorders

Copyright © 2009 John Wiley & Sons, Ltd.

inconsistent with regard to CC sub-regions. For example, Piven *et al*. [2] reported reductions in the size of the body and posterior regions of the CC in autistic patients, Hardan *et al*. [3] found significant differences in anterior regions, and Vidal *et al*. [1] found reductions in genu and splenium as well as the total CC area. A detailed summary of CC abnormalities in autism can be found in [4]. The inconsistency of the results may be due to factors such as the sample size, subject age and gender, and specific diagnosis. Particularly, heterogeneity within the autism diagnosis obscures the genetic basis of the disorder [5]. Recently, Miles *et al*. proposed a new definition of autism subgroups, which divided autism into essential autism and complex autism [5]. Limiting studies of brain morphology to individuals with essential autism decrease the background noise of structural variation and allow the analysis of the more uniform population [5]. He *et al.* [6] first adopted this definition and compared the shape difference between subjects with essential autism and controls, although their sample size was conspicuously small. In this paper, we also focus on essential autism, which will greatly reduce the heterogeneous factors.

Quantitative morphologic assessment of individual brain structures is often based on volumetric measurements and shape analysis. Shape analysis has gained an increasing amount of interest from the neuroimaging community because it can precisely locate morphological changes in the pathological structures, which cannot be reflected in volume measurements. A significance map is often computed in shape analysis, which tells how significant the difference is between two groups of structures at each location. However, shape analysis gives little description with respect to the phenotype, which is directly linked to the genetic basis of the diseases. A phenotype is the appearance of visible characteristics of an organism produced by its genes and their interaction with the environment; a phenotypic trait is a visual category of phenotypic variation [7]. Under this definition, CC volume is a trait, but agenesis of the CC is a phenotype. Most of the previous works only focus on the volume measurement. However, there are many other traits that can be defined based on the characteristics of the CC shape.

Shape morphology of the CC in autism has been studied in [1, 6]. In [1], CC thickness (the distance from a medial line) at each surface point was compared between patients and controls. In [6], an average CC model was used as a template and the distance to the template at each point was compared between two groups. However, the shape analysis in both was still in a 2D manner, because the comparison was performed on a contour-by-contour basis.

This paper gives a comprehensive pipeline of the analysis of the CC with respect to the shape, morphology and phenotypic traits in essential autism (Figure 1). The 3D model of the CC is reconstructed from 2D contours of nine sagittal slices as in [1]. We use a newly developed semiautomatic method [8] to segment the CC from 2D MR images. Compared with the manual tracing method in most previous work, our method is faster and more accurate, which will facilitate the following analysis. In the phenotypic trait analysis, volumes of the CC and five sub-regions are compared in a way similar to [1]. CC thickness at each region border is also compared. Moreover, an oriented bounding rectangle of the 2D CC on sagittal magnetic resonance imaging (MRI) is constructed, and the length, width and ratio (length/width) of the bounding rectangle are the MRI traits to be compared between autism and control groups. Since the oriented bounding rectangle of an object is the minimum rectangle that encloses this object, the measurements of the bounding rectangle can give both size and shape information. In the shape analysis, we directly compare the 3D coordinates at each surface point of the CC model using Hotelling T^2 two sample tests [9]. In order to perform this comparison, point correspondence among different individual models must be established. We develop a new planar conformal mapping based on the methods in [10, 11] to map the surface onto a planar domain and thus find a one-to-one point correspondence among different

Copyright © 2009 John Wiley & Sons, Ltd.

DOI: 10.1002/cnm

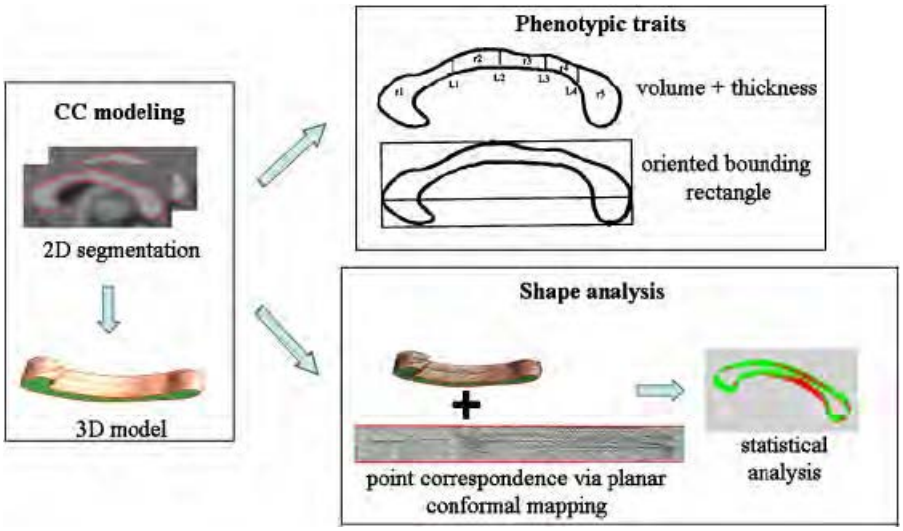

Figure 1. Schematic view of the entire procedure.

models. The results of this paper show both the differences in the phenotypic traits measurements and the visualization of local shape differences between patients and controls.

2. METHODS

This section describes the details of our methods, including CC segmentation, phenotypic trait measurement and statistical shape analysis. The entire procedure can be summarized in the following steps:

1. For each subject, CC contours are segmented from mid-sagittal slice and four adjacent slices on each side, and a 3D model of the CC is constructed by contour stitching.
2. CC volumes and measurements of the oriented bounding box are computed, and differences of these measurements are compared between patients and controls using t-tests.
3. Each CC model is mapped onto a planar domain and re-triangulated to establish the point correspondence among different models.
4. Spatial alignment of all CC models is performed using Procrustes analysis.
5. 3D coordinates at each surface point are compared between patients and controls using Hotelling T2 tests, which results in a significance map of group differences.

The following subsections will describe each step in details.

2.1. CC modeling

We start with slice-by-slice segmentation and stack the 2D curves to make a 3D model. Because, it is more straightforward to verify the accuracy of 2D results slice-by-slice, this method provides better results as opposed to direct 3D segmentation and validation. Mid-sagittal slice and four adjacent slices on each side are used for CC segmentation. The local shape variation of the CC is

Copyright © 2009 John Wiley & Sons, Ltd.

DOI: 10.1002/cnm

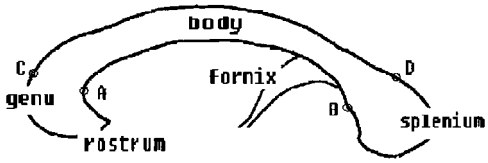

Figure 2. Four parts of the CC boundary: anterior (AC), upper body (CD), posterior (DB), lower body (BA) (image modified based on original illustration from [12]).

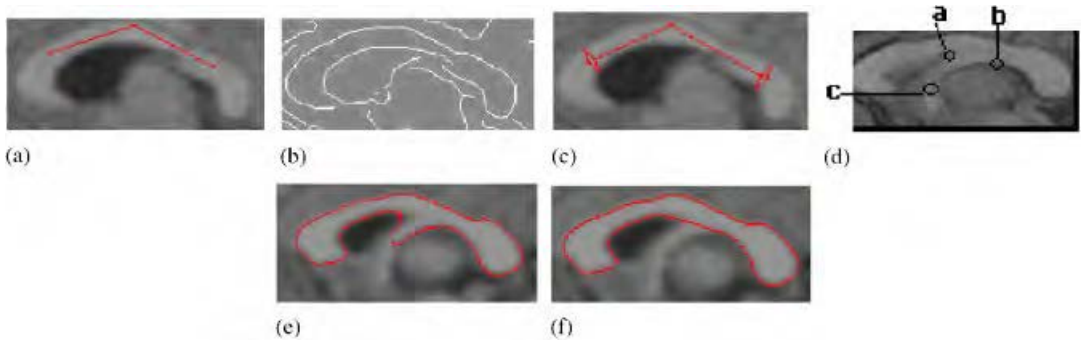

Figure 3. (a) User-initialized polyline; (b) the edge map; (c) the completed seed contour; (d) distinct points around the fornix; (e) the result without fornix removal; and (f) the result with fornix removal.

dramatic, and parts of the CC may be narrow or have bumps. The most challenging problem is the existence of the fornix, which is a thin structure that may or may not contact the CC in sagittal MR images; it is almost the same intensity as the CC. He *et al.* proposed a part-based semiautomatic method [8] to segment the CC on sagittal slices, which can effectively overcome most of the challenges. The novelty of this method is dividing the CC boundary into four parts connected by four sensor points (Figure 2). The user initializes a polyline inside the CC region by three mouse clicks (Figure 3(a)), and a seed contour consisting of four parts is automatically generated by point tracing on the edge map (Figure 3(b) and (c)). The details of the seed construction can be found in [8]. The seed will then automatically deform according to active contour evolution, but each part has its own motion law. The contour evolution mechanism can be found in [8].

The fornix tip can also be removed by automatic fornix detection [8]. Since we know the fornix always appears beneath the body of the CC, we only need to search along the lower boundary to detect it. There are three distinct points around the fornix (Figure 3(d)). The fornix dip is removed by connecting points a and b. The final result on one sagittal slice is shown in Figure 3(f), compared with the intermediate result with the fornix dip in Figure 3(e). The quantitative evaluation of the segmentation results is performed in [8], which shows high accuracy of this method.

Since the CC shapes on adjacent slices do not differ too much, we apply the segmentation method on mid-sagittal slice and the result is used as the seed for its two neighbor slices. After slight deformation, the boundary curves on these two slices can be obtained and each one is again used as the seed of its next adjacent slice.

Contour stitching is performed to create the 3D CC model of each subject. Since the segmentation method can keep track of the four sensor points on the CC boundary, the point correspondence

Copyright © 2009 John Wiley & Sons, Ltd.

DOI: 10.1002/cnm

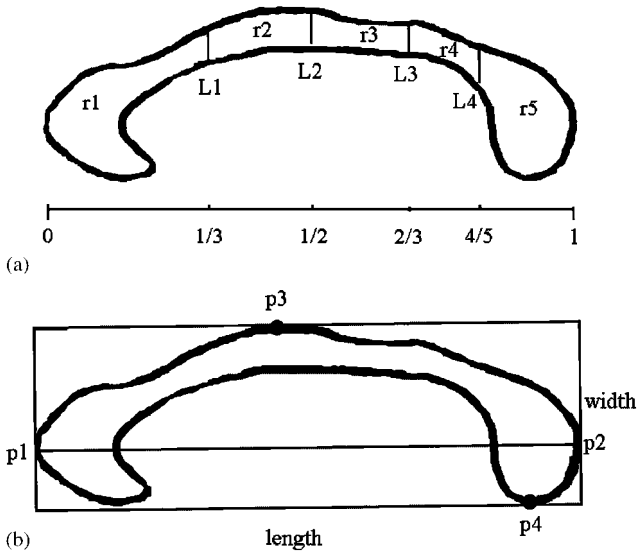

Figure 4. (a) Partition of the CC: r1—anterior third; r2—anterior body; r3—posterior body; r4—isthmus; r5—splenium and (b) bounding rectangle of the CC.

problem can be simplified by first matching the sensor points among contours [6]. After matching the sensor points, the four parts are implicitly matched among contours. We only need to match the individual points within each part. The details of matching the sensor points and the inner points of the four parts can be found in [6].

By connecting the matched point pairs between adjacent contours, the 3D mesh is created. A tangential Laplacian smoothing [13] is performed to maintain a good node distribution of the model. The reconstructed model is shown in Figure 5.

2.2. Phenotypic traits

Volumes of the CC and its sub-regions are computed similar to that in [1]. The CC is divided into five regions along anterior–posterior line (Figure 4(a)). To find the anterior–posterior line, we calculate the distance between every two points on the CC boundary, and find the pair of points with the longest distance (p1 and p2 in Figure 4(a)). The line connecting these two points is the anterior–posterior line. The five regions are defined the same as in [1]. For simplicity, we label them from r1 to r5 as shown in Figure 4(a). Areas are computed in pixels for each 2D segmented CC, and the areas of nine slices are summed to generate the voxel count of the 3D model. The raw volume is the multiplication of the voxel count and the voxel size in mm^3. To take into account the effect of the brain volume, we normalize the raw CC volume by the total brain volume (TBV) and the intracranial volume (ICV), respectively. TBV includes gray matter and white matter and excludes ventricles [14], and ICV is the sum of white matter, gray matter, and inner and outer cerebrospinal fluid spaces [15]. A choice can be made between using TBV or ICV as an adjustment factor [14], but our results show that the two choices do not make any difference. The brain volumes, raw and scaled volumes of the CC and the five regions are compared between patients and controls using t-tests.

Copyright © 2009 John Wiley & Sons, Ltd.

DOI: 10.1002/cnm

We explore additional phenotypic traits based on the oriented bounding rectangle of the CC. To construct the rectangle, we first find points p1 and p2 as mentioned above. On each side of line p1p2, we find a point on the CC boundary which has the maximum distance to line p1p2 (p3, p4 in Figure 4(b)). The bounding box is a rectangle whose long edges pass p3 and p4, respectively and are parallel to line p1p2, and whose short edges pass p1 and p2, respectively (Figure 4(b)). We measure the length, width and aspect ratio (length/width) of the bounding rectangle on each 2D slice and average them across the nine slices. The shape of the bounding box depends on both the size and the shape of the CC, so these traits can reflect both size and shape information of the CC. We also compute the thickness at the border of every two sub-regions, which is the length of each dividing line (L1–L4 in Figure 4(a)). With a little abuse of notation, we denote the thickness at each dividing border as L1–L4. The thickness at each border is averaged across the nine slices. The average measurements of the bounding box and the thickness are compared between patients and controls using t-tests. To account for the brain volume effect, we scale the above raw measurements by the cubic root of TBV and ICV, respectively. Since these measurements are in millimeter, this scaling makes the units consistent. These scaled measurements are also compared between patients and controls.

2.3. Point correspondence via planar conformal mapping

Conformal parameterization has been explored intensively as a potential approach to the matching and analysis of brain data. It maps the brain surface into regular and more simple domains and carries out the analysis on the parameter domain. Gu *et al*. [11] used spherical conformal map to match cortical surfaces, where they parameterized the genus zero closed surfaces by spheres. Unlike their data, the CC surfaces we are studying have two boundaries, which are the 2D CC contours of the two end slices. Inspired by [10], we design a planar conformal mapping method. In order to find point correspondence among different CC surfaces, we first parameterize each CC surface using a planar domain, and then align the parameterization in the planar domain so that surface points across different objects posses the same parameterization. Finally, the aligned parameterization in the planar domain is mapped back onto the original surfaces (Figure 5).

Among all the CC models an arbitrary model is chosen as the target surface, and the corresponding points on the other models (source surfaces) are to be established to match the points on the target surface. We conformally flatten the target surface M onto a planar domain M', which is a rectangle with the two boundaries γ_1 and γ_2 mapped to the upper and lower long edges. In order to parameterize the given surface with a planar domain, we need to construct a special

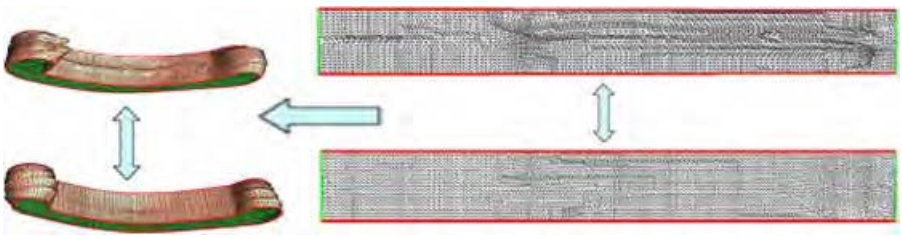

Figure 5. Illustration of establishing point correspondence via planar conformal mapping: two individual CC models (left) and their planar domains (right).

Copyright © 2009 John Wiley & Sons, Ltd.

DOI: 10.1002/cnm

holomorphic one-form $\tau+\eta\sqrt{-1}$, such that its integration around the boundaries has a real part with a constant period, while the integration along a path from one boundary to the other has a constant imaginary part. To get the imaginary part η, we need to compute a harmonic function f by solving a Dirichlet problem:

$$\begin{aligned} \Delta f &= 0 \\ f|_{\gamma_1} &= 1 \\ f|_{\gamma_2} &= 0 \end{aligned} \tag{1}$$

η is the gradient of f and the real part τ is the conjugate of η. In our implementation, we first convert η into a piece-wise constant vector field υ_η sampled at each face; rotate υ_η by 90° around the face normal, and turn the rotated vector field into the one-form τ. Choosing an appropriate starting point, we can integrate the holomorphic one-form $\tau+\eta\sqrt{-1}$ on M. Taking the real and imaginary parts of the integration to be y and x coordinates, respectively, we get a horizontal strip that is periodic along the X direction. Cutting the strip along the vertical line $x=0$, we get the final planar domain M', where the upper and lower side corresponds to the two boundaries in the original mesh M. The map from M to M' is conformal; the height–width ratio of the rectangle is a conformal invariant of the original surface. In our experiments, we always re-scale the rectangle uniformly along the X and Y directions so that the width equals to 2π. As a consequence, the intrinsic structure is solely reflected by the height of the rectangle for our cases.

The same method is used to map each source surface onto its planar domain. After that, we compute the map between the target planar domain and each source planar domain. In our case, a reasonable map should satisfy two constraints. First, each boundary of the source surface should be aligned with the corresponding boundary of the target surface. In the rectangle domain, we need to map the upper (lower) edge of the source rectangle to the upper (lower) side of the target rectangle. As mentioned before, the width of the rectangle is always equal to 2π, while the height may be different from model to model. Therefore, we may need to re-scale one rectangle along the Y direction to align with the other rectangle. In our experiments, all the rectangles have similar heights, so the re-scaling factor is very close to one and therefore would not hurt the conformality of the map too much. Even in the case of a bigger re-scaling factor, the map is still affine and therefore harmonic, which is already strong enough for our purpose. The second constraint is to align the 'bending corner' (i.e. point c in Figure 2(d)) across two surfaces. In order to make the mapping process easier, we choose the bending corner to be the starting point used in the integration of the holomorphic one-form. As a consequence, in the planar domain the bending corner will appear at the vertical cutting side. Aligning the two rectangles along their left and right sides, the bending corners will be automatically matched. Since all the rectangles have the same width 2π, we do not need to re-scale any of them along the X direction.

Once the source rectangle is totally aligned with the target one, we get a map F' between two planar domains. For each vertex v on the target rectangle, there is a point $F'(v)$ in the source rectangle, which may lie inside a triangle, on an edge or at a vertex. Without loss of generality, we represent the point as a linear combination $F'(v)=b_0v_0+b_1v_1+b_2v_2$, where v_i is the vertex of the resident face and b_i the corresponding barycentric coordinate. The map F' between two planar domains induces a map F between the two original surfaces. Namely, each vertex v in the target surface corresponds to a point $F(v)=b_0v_0+b_1v_1+b_2v_2$ in the source surface. To facilitate later processing, we re-sample the source surface using these points as vertices, and re-triangulate

Copyright © 2009 John Wiley & Sons, Ltd.

DOI: 10.1002/cnm

the source surface with the same connectivity as that of the target surface. Therefore, each point on the source surface has a correspondence on the target surface, and the two surfaces have the same triangulation.

The same method is used to align each source planar domain with the target planar domain, and to re-triangulate the source surface. In this way, the point correspondence among all the surfaces is established through the target surface.

2.4. Spatial alignment

Before the shape comparison, rigid-body Procrustes Analysis [16] is performed on each 3D mesh across subjects in order to eliminate the shape differences caused by translation, rotation and scaling. The algorithm can be summarized as follows:

1. Select one shape to be the approximate mean shape (e.g. the shape of the first subject).
2. Align each shape with the approximate mean shape:
   (a) Translate each shape so that its centroid is at the origin.
   (b) Normalize each shape X by a scale factor $s = \|X\|$, where X is the coordinate matrix consisting of row vectors of the coordinate of each point after translation.
   (c) Rotate each shape to align with the newest approximate mean shape. The details of the rotation algorithm can be found in [16].
3. Calculate the new approximate mean shape from the aligned shapes. If it is different from the one in step 2, return to step 2.

2.5. Statistical testing of group mean differences

The difference in the size of the CC has been eliminated in the spatial alignment, so the shape analysis only reveals pure shape difference in local CC area between patients and controls. In the local shape analysis, difference between groups at every surface location is tested (Figure 6). This can be done in two main ways [9]. One way is to analyze the local difference to a template, which

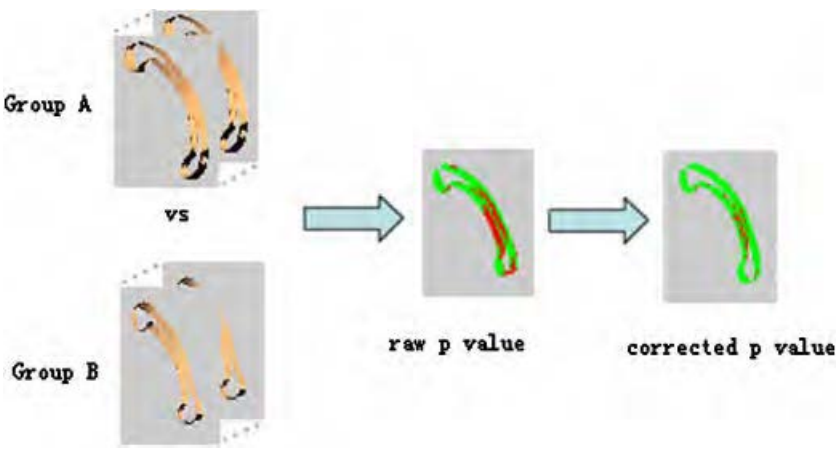

Figure 6. Schematic view of the test procedure.

Copyright © 2009 John Wiley & Sons, Ltd.

DOI: 10.1002/cnm

is usually the mean of the two groups. Student t-test can be used to test the local significance and He *et al*. [6] used this method. The main disadvantage of this method is the need to select a template, which introduces an additional bias. The other method is to directly analyze the spatial location of each point, and we apply this method in our study. No template is needed in this approach and multivariate statistics of the (x, y, z) location are used. Hotelling T^2 two-sample metric is used to measure how two groups are locally different from each other. We use a modified T^2 metric instead of the standard one, because it is less sensitive to group differences of the covariance matrixes and the sample size [9]. This metric is defined as

$$T^2 = (\mu_1 - \mu_2)' \left((1/n_1) \sum_1 + (1/n_2) \sum_2 \right)^{-1} (\mu_1 - \mu_2) \tag{2}$$

where $\sum_1$ and $\sum_2$ are the covariance matrices of the two groups. Since comparisons are made at thousands of CC surface points, a permutation test is, therefore, used to confirm the significance of the overall differences in the statistical mapping result adjusting for multiple comparisons [17]. Suppose we have two groups A and B whose sample sizes are n_{A} and n_{B}, the permutation scheme can be stated as follows:

1. Calculate the test statistic (in our case, T^2) between A and B, denoted as S_0.
2. The observations of A and B are pooled. From the pooled values, n_{A} observations are sampled without replacement to form group A, and n_{B} observations are sampled to form group B. The test statistic between the two new groups is calculated.
3. Repeat the sampling process (permutation) in step 2 for M times. The test statistic in jth permutation is denoted as S_j.
4. The proportion of S_j's, which are greater than S_0 is the p-value.

M is a large number with the maximum value of

$$\binom{n_{\mathrm{A}} + n_{\mathrm{B}}}{n_{\mathrm{B}}}$$

The resulting p-values generate a significance map that locates significant shape differences between the two groups. Both raw and corrected p-values are shown in the experiment.

We also perform a global shape analysis, where the average of the local Hotelling T^2 metrics across the whole surface is calculated for each subject, and the p-value is computed in the same way as for the local testing. No permutation is needed since there is only one test.

3. RESULTS

3.1. Subjects and data

Thirty patients with essential autism participated in this study. All patients met the DSM-IV criteria [18] as well as autism diagnostic interview-revised (ADI-R) and ADOS algorithm criteria. The distinction between essential and complex autism is based on the presence of generalized dysmorphology, which is indicative of an insult to early embryologic development and has been previously reported [5]. Children with a known disorder such as Fragile X, Tuberous Sclerosis, a chromosome abnormality or severe prematurity with brain damage and children with IQs/DQs

Copyright © 2009 John Wiley & Sons, Ltd.

DOI: 10.1002/cnm

Table I. Volume measures.

CC measure	Patients	Controls	p-value
TBV (cm^3)	1421.9±299.4	1313.6±336.0	0.09
ICV (cm^3)	1460.4±308.3	1348.3±345.5	0.09
Raw measures	(mm^3)		
Total CC	4229.1±755.3	4727.7.0±971.4	0.01
r1	1754.2±321.3	1939.5±367.9	0.02
r2	474.4±103.9	556.1±142.9	0.008
r3	439.7±123.1	505.1±139.9	0.03
r4	404.6±108.3	458.8±140.8	0.05
r5	1153.3±227.7	1263.5±275.7	0.05
Scaled by TBV	($\times 10^{-4}$)		
Total CC	31.0±9.3	37.0±8.1	0.004
r1	13.0±3.5	15.1±3.1	0.004
r2	3.4±1.0	4.3±1.0	0.001
r3	3.2±1.2	3.9±1.0	0.009
r4	2.9±1.0	3.6±0.9	0.01
r5	8.6±2.9	10.1±2.4	0.02

less than 40 will be excluded. Five healthy people recruited from the NIH Human Brain Project participated as controls. Besides, we also obtained MR images of 23 controls from IBSR database [19]. The age range of all participants is 3–30.

MR images of our patients and controls were obtained from our autism aesthesia protocol, which included intravenous infusion of protocol to insure image quality. Axial, coronal and sagittal T1-weighted images were acquired using the Siemens Symphony 1.5 T scanner with the following parameters: TR = 35 ms, TE = minimum ms, NEX = 1, flip-angle = 30°, thickness = 1.5 mm, field of view = 22 cm, matrix = 512 × 512. The data obtained from IBSR were T1-weighted MR images with 3.1 mm thickness. Each brain volume was interpolated to 0.9 mm isotropic voxels.

3.2. Phenotypic trait measurements

Table I shows the t-test results of the volumes. The mean TBV and ICV of the patients are greater than those of the controls, but the p-values do not reveal any significance in this difference ($p>0.05$). The raw measures of the CC volume and its sub-regions show that the patient's volume is significantly smaller than the controls ($p<=0.05$), especially in the region r2 (anterior body). The comparison of the scaled measures by TBV and by ICV shows similar results, both of which augment the significance of the difference. Table I only shows the results of TBV normalization.

Table II gives the t-test results of the traits regarding the bounding rectangle and the thickness. In the raw measures, the patients have significantly reduced length and aspect ratio of the bounding rectangle, while other traits do not show any significance in the difference between patients and controls. When scaled by the cubic root of TBV, the length of the bounding rectangle keeps its strong significance and the width still shows no significance in the group difference. The p-values of the difference in thickness are decreased but none of them reach the significance level (0.05). The difference in L2 between patients and controls is close to significant, which is consistent with the volume measurements since the anterior body displays most significant difference. The comparison shows similar results when the measurements are scaled by the cubic root of ICV, and Table II only shows the results of TBV normalization.

Copyright © 2009 John Wiley & Sons, Ltd.

DOI: 10.1002/cnm

Table II. Phenotype traits.

CC measure	Patients	Controls	p-value
Length	66.2±4.8	72.1±5.0	$<10^{-4}$
Width	24.0±3.0	23.6±3.6	0.33
Length/width	2.78±0.3	3.11±0.49	0.002
L1	5.91±1.13	6.09±1.19	0.28
L2	5.40±1.18	5.76±1.35	0.14
L3	5.11±1.35	5.29±1.53	0.31
L4	7.53±1.76	7.77±2.06	0.32
Scaled by TBV			
Length	0.59±0.05	0.66±0.06	$<10^{-4}$
Width	0.21±0.02	0.22±0.03	0.35
L1	0.053±0.011	0.056±0.010	0.14
L2	0.048±0.011	0.053±0.011	0.07
L3	0.045±0.012	0.048±0.013	0.20
L4	0.067±0.016	0.071±0.017	0.22

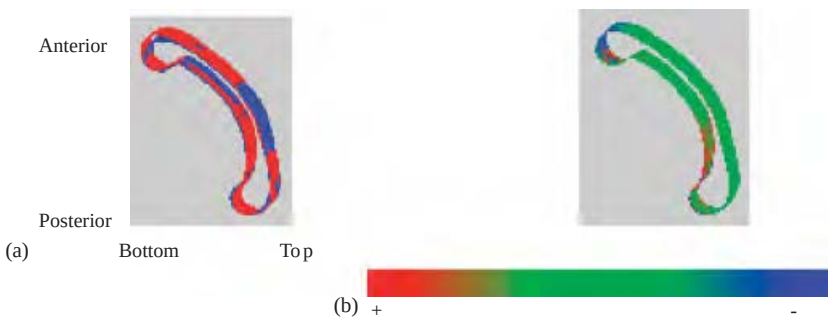

Figure 7. (a) Overlaid average structures (blue: controls, red: patients) and (b) distance map between the two averages.

3.3. Group mean difference map

Figure 7 gives a descriptive visualization of the group difference. The overlaid average CC structures are shown in Figure 7(a). Figure 7(b) shows the signed distance map between the two average structures rendered on an overall average shape, where the negative distances indicate that the patients' structure is outside the controls and the reverse is for the positive distances. The anterior is more projected and the posterior is more inward in the patients' structure. The posterior body and isthmus are thinner in the patients' structure.

3.4. Statistical testing results

The significance maps of the raw and corrected p-values are shown as color coded p-values in Figure 8. Smaller p-values indicate larger statistical significance. A two-tailed alpha level of 0.05 is chosen as the significance threshold. Figure 8(a) is the significance map of raw p-values, which reveals significant difference in the anterior most, anterior body, isthmus and posterior bottom.

Copyright © 2009 John Wiley & Sons, Ltd.

DOI: 10.1002/cnm

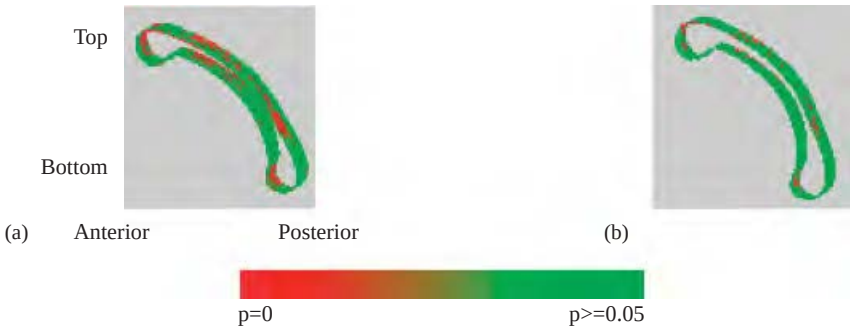

Figure 8. Significance map: (a) raw p-values and (b) corrected p-values.

This result is an optimistic estimation. The permutation result is shown in Figure 8(b), which retains part of the significance in the raw map. The global shape analysis has a p-value of 0.008.

4. CONCLUSION AND DISCUSSION

Based on the new definition of autism subgroups, we investigate the CC abnormalities in essential autism, and exclude the complex autism group in order to find more homogeneous results. We use a semiautomatic method to segment 2D CC boundaries, and 3D surfaces are reconstructed by contour stitching. Regional volumes and additional phenotypic traits based on the oriented bounding rectangle of the CC are compared between patients and controls. A newly developed planar conformal mapping is used to parameterize the 3D surfaces. Shape comparison is conducted at each surface location using Hotelling T^2 test followed by a permutation test.

In the volume comparison, no significance is found in TBV or ICV between patients and controls, but the non-significant trend for an increase in the brain volumes in patients is consistent with the most previous literatures [2, 3, 20]. The significant reduction in the total CC volume in the patients is consistent with [1]. We find significant reduction in each sub-region of the CC in the patients, but in [1] only a significant reduction in the anterior third was found. Besides the traditional volume test, we also conduct some tests based on the oriented bounding rectangle, which has not been done in the previous work. The length, width, and aspect ratio of the bounding rectangle are measured for comparison. We find significant reduction in the CC length and ratio in the patients, but the difference in the width is far from significant. This gives us some insight that the decrease in the CC volume is caused by the decrease in the anterior–posterior length more than the top–bottom length.

In the shape analysis, the distance map reveals more projected anterior most and inward posterior bottom, as well as the thinner body of the CC in the patients. The raw significance map suggests significant differences in the anterior most, anterior body, isthmus and posterior bottom, while the corrected significance map retains part of the significance in each region shown in the raw map. Table III gives a summary of the findings in [1, 6] and our study regarding the shape differences between autism and control groups. First, our results are similar to [1] in the posterior part, but the result in [6] is opposite. This may be accidental because there is no significance in their result. Second, our result on the anterior part is consistent with [6] but contrary with [1]. This may be

Copyright © 2009 John Wiley & Sons, Ltd.

DOI: 10.1002/cnm

Table III. Comparison of the CC shape analysis in different studies.

	Body		Anterior		Posterior	
CC regions	Shape	Significant	Shape	Significant	Shape	Significant
[1]	Less arching	No	More inward	Yes	More inward	Yes
[6]	Less arching	Yes	More projected	No	More projected	No
Our study	Posterior thin	Yes	More projected	Yes	More inward	Yes

explained by the population because [6] and our study exclude both the complex autism while [1] does not. Both [1, 6] have found less arching in the body of the CC in autistic patients, but we have found the body thinner in the posterior half. He *et al*. [6] and our study both find significance in the shape changes of the body, although the changes are different.

The results of this study need to be interpreted cautiously because of several limitations. First of all, the age range of our sample is very wide, which may have some effect on the CC measurements. Second, we exclude the complex autism group as it was done in [6]. However, with the improvements in the surface matching and statistical testing methods compared with [6], our results are more convincing than [6].

In conclusion, patients have a trend for a reduction in the volumes of the total CC and each subregion. Further experiment with larger sample size needs to be done to confirm the significance of these size differences. New phenotypic traits based on the oriented bounding box are studied. The decrease in the anterior–posterior length is found to be the main reason for the CC size reduction. A new surface matching technique is used for shape comparison. The permutation results show significant difference in the anterior most, anterior body, isthmus and posterior bottom. Further studies on different subgroups within autistic patients need to be done, such as male vs female and complex vs essential. These findings will better explain the inconsistent results caused by the population.

ACKNOWLEDGEMENTS

Some of the authors of this paper are supported in part by a research scholarship funded by the Thompson Center for Autism and Neurodevelopmental Disorders. We are very grateful for Dr Evan Boote and Chris Jones for helping us in obtaining the MRI data used in this study.

REFERENCES

1. Vidal CN, Nicolson R, DeVito TJ, Hayashi KM, Geaga JA, Drost DJ, Williamson PC, Rajakumar N, Sui Y, Dutton RA, Toga AW, Thompson PM. Mapping corpus callosum deficits in autism: an index of aberrant cortical connectivity. *Biological Psychiatry* 2006; **60**(3):218–225.
2. Piven J, Bailey J, Ranson BJ, Arndt S. An MRI study of the corpus callosum in autism. *American Journal of Psychiatry* 1997; **154**:1051–1056.
3. Hardan AY, Minshew NJ, Keshavan MS. Corpus callosum size in autism. *Neurology* 2000; **55**:1033–1036.
4. Brambilla P, Hardan A, di Nemi SU, Perez J, Soares JC, Barale F. Brain anatomy and development in autism: review of MRI studies. *Brain Research Bulletin* 2003; **61**:557–569.
5. Miles JH, Takahashi TN, Bagby S, Sahota PK, Vaslow DF, Wang CH, Hillman RE, Farmer JE. Essential vs complex autism: definition of fundamental prognostic subtypes. *American Journal of Medical Genetics* 2005; **135A**:171–180.

Copyright © 2009 John Wiley & Sons, Ltd.

DOI: 10.1002/cnm

6. He Q, Duan Y, Miles JH, Takahashi TN. Statistical shape analysis of the corpus callosum in subtypes of autism. *IEEE 7th International Symposium on Bioinformatics and Bioengineering*, Boston, MA, U.S.A., 14–17 October 2007.
7. Shyu C, Green JM, Lun DPK, Kazic T, Schaeffer M, Coe E. Image analysis for mapping immeasurable phenotypes in maize. *IEEE Signal Processing Magazine* 2007; 115–118.
8. He Q, Duan Y, Miles JH, Takahashi N. A context-sensitive active contour for image segmentation. *International Journal of Biomedical Imaging* 2007; **2007**:8. Article ID 24826, DOI: 10.1155/2007/24826.
9. Styner M, Oguz L, Xu S, Brechbuehler C, Pantazis D, Levitt JJ, Shenton ME, Gerig G. Framework for the statistical shape analysis of brain structures using SPHARM-PDM. *Insight Journal—2006 MICCAI Open Science Workshop*, 2006.
10. Gu X, Yau S. Global conformal surface parameterization. *Proceedings of the 2003 Eurographics/ACM SIGGRAPH Symposium on Geometry Processing*, 2003; 127–137.
11. Gu X, Wang Y, Chan TF, Thompson PM, Yau S-T. Genus zero surface conformal mapping and its application to brain surface mapping. *IEEE Transactions on Medical Imaging* 2004; **23**(8):949–958.
12. McInerney T, Hamarneh G, Shenton M, Terzopoulos D. Deformable organisms for automatic medical image analysis. *Medical Image Analysis* 2002; **6**:251–266.
13. Wood Z, Desbrun M, Schroder P, Breen D. Semi-regular mesh extraction from volume. *Proceedings of the Conference on Visualization '00*, 2000; 275–282.
14. O'Brien LM, Ziegler DA, Deutsch CK, Kennedy DN, Goldstein JM, Seidman LJ, Hodge S, Makris N, Caviness V, Frazier JA, Herbert MR. Adjustment for whole brain and cranial size in volumetric brain studies: a review of common adjustment factors and statistical methods. *Harvard Review of Psychiatry* 2006; **14**(3):141–151.
15. Wolf H, Kruggel F, Hensel A, Wahlund L-O, Arendt T, Gertz H-J. The relationship between head size and intracranial volume in elderly subjects. *Brain Research* 2003; **973**(1):74–80.
16. Ross A. Procrustes analysis. *Technical Report*, Department of Computer Science and Engineering, University of South Carolina, SC, 2004. Available from: www.cse.sc.edu/∼songwang/CourseProj/proj2004/ross/ross.pdf.
17. Nicolson R, Devito TJ, Vidal CN, Sui Y, Hayashi KM, Drost DJ, Williamson PC, Rajakumar N, Toga AW, Thompson PM. Detection and mapping of hippocampal abnormalities in autism. *Psychiatry Research*: *Neuroimaging* 2006; **148**:11–21.
18. American Psychiatric Association. *Diagnostic and Statistical Manual of Mental Disorders* (4th edn). Text revision, American Psychiatric Association: Washington DC, 2000.
19. http://www.cma.mgh.harvard.edu/ibsr/.
20. Palmer SL, Reddick WE, Glass JO, Gajjar A, Goloubeva O, Mulhern RK. Decline in corpus callosum volume among pediatric patients with medulloblastoma: longitudinal MR imaging study. *American Journal of Neuroradiology* 2002; **23**:1088–1094.

Copyright © 2009 John Wiley & Sons, Ltd.

DOI: 10.1002/cnm

Facial Phenotypes and Subgroups in Children with Autism Spectrum Disorders

Kristina Aldridge[1 2], Kimberly K. Pope[1], an D. George[1], Cheryl A. Hi l[1] , T. Nicole Ta ahashi[2], Judith H. Mil s[2], Ye Duan [3]
Departmen of Pat o og and Ana omi al Sciences, [2]T ompson Cen er or A ism an Neu odevelopmen al Disorde s, Depa tmen of omputer Sciences
University f Miss uri-C lumbia

NT ODUC ON

Au sm spec rum iso de s (D a e curren ly def ne b a om on be a io al phe o pe, with resea h bei g in reasi gl foc sed o fin i g bo a gene ic a se n a eu oa a omi al basi for he be a io ph no pes in SD. Sinc h b ologi al b in dev lops in onc t wi h he face i is po sible at the a ges in he b ain mo p o ogy are efle ted in i ferences i soft issue mo pho og of he face in c ildren with SD.

In this study we test t o h potheses:

. Children with SD dis la a istin fa ia phe ot pe as ompared o pi ally-d ve oping children.

2. There are s bg oups of facial phe o pes <u>within</u> SD t at may represent dis rete bio ogi al s bg o ps.

MATERIA S AND ME HODS

igure Su aces a q ired b the 3 MD s stem. The su fa es are s own at ifferen o ie ta io s o de onst ate he 3-D a ure of the a a.

he s udy sample i luded 8- o-12 yea -ol bo s iag osed with au ism spect um diso d r N=6) and t pi a ly-deve pi g ge-match bo s N=4) 3-D st r op o ogrammet ic im ges were a q ired si g he 3 MD ra ial s stem at he T o p on Cente for Au ism and Neu odeve opme al Di orde s fo lowi g pp oved B p o o ol igure).

Se ente 3-D anth opomet ic fa ial landmar s w r ollected f om the i ages ac o s he orehead eyes, se and out regio s igure) ol owi F r as]. E or st ies in i ate at these poi s a be o lected ith pr i io and ac u acy [ ]. Landmark oo di ate a a were a al zed si g Eu idea Distance Ma ix a ses DM), ic o pare for s between o g o ps of in i id a s 3]. A prin ipal or i ates a l si ppli a ion of DMA P OO D) tes s o poten ial luste s of indi id als base on hei andmark a a.

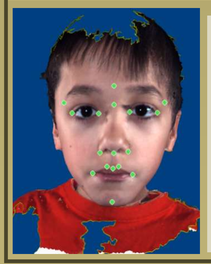

igure 2. andmar s o lected f om the 3 MD images See a as [ ] or an rk defi i io s.

Fi a ly we teste for o re a io s a o g res l s f om P OO D a al ses and i i al phe ot pic c a acte s.

R SULTS

1) A al ses s ow at c i dre iag osed with SD de o st ate ifferen es i fa i l o p ology ompared o pi a ly deve opi g c ildren (igure 3).

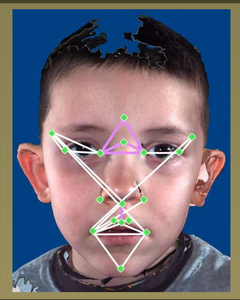

g e 3. Me su es t are signifi an ly ifferen i bo s wi h SD as o p red o t pi al y de el pi g c ildren. W ite lin s in icat m asu s t a are a ge in ildren with SD, w ile pu ple ines represent easu es a are sm lle in c ildren with SD.

) P OO D r s l s in i at s bg o ps of c ildr n with ASD a are differe f o both t e other c ildren with SD and pi a ly deve o i g ildren (igure 4 . hese es l s o ot eflect orre a io s with ge or head ize.

F gure 4. a) P OO D re l s. **b)** Measu es d s i s i g S bg o p Pu ple ines in i a e me sures posi i ely orr at d with A is 1, w il w it lin s ar n ga i ly orre ated wi h xis 1. Measures i ti g is i g S bg o p 2 Pu ple ines i i te measures osi ively or elated i h Axis 2, w ile w ite lines are nega ively orre ated with Axis 2.

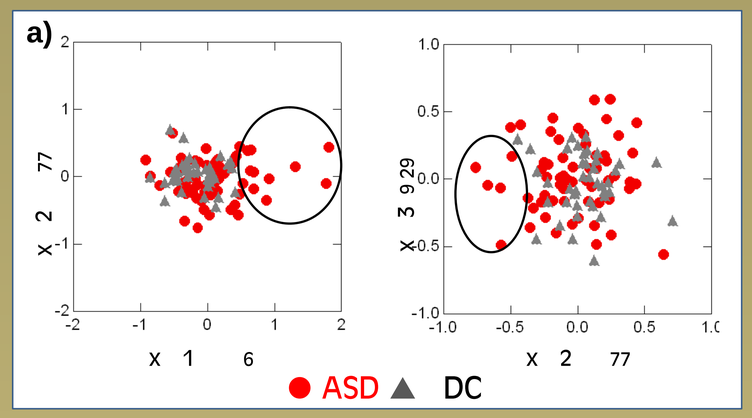

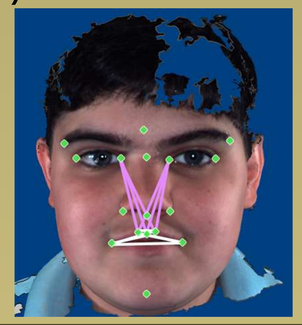

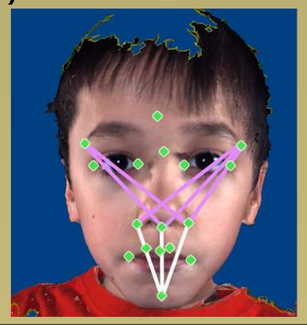

R SUL S, ont'd.

3) We find sta is i a l sig ifi nt o rela io s between s bg o p me be s ip and li i al and be a io al c a acte is i s able).

T bl . Sig ificant orr a io s ith s bg o p me be s ip as o pared o he ain SD g o p.

	S bg o p 1	Subg o p 2
D ag os s	↑ Au st c D sord r	↑ sp g s
Severity	High S Q	Mod ate S Q
Q	ower	Higher
Att n ion	High r BCL	ow r BCL
a g ag	- - - - - - - - - -	H gh r
amily h s ory	- - - - - - - - - -	↑Anxi ty D sord r
Oth r	↑ s zur s	↑ lumsin ss

CONCL S ONS

Ou h pothe es:

. C ildren ith SD i pl a istinc fa ial phe o pe as ompared o t i ally-develo i g c ildren Yes but t is phe o pe is s b le and ig ly o a ized.

. There are s bg o ps of a ial phe ot pes <u>wit in</u> SD t at may r pres nt iscr t biologi al s bg o ps. es a least t o. S bg o ps of bo s wit SD s ow istinc fa ia phe o pes t at orre ate with i i al and be a io al phe o pes.

Diff renc s i fa ial o p ology may r fl c altera ions in he deve opmen of the b ain du i g pre a al eve opment i c ildren ith SD Our es l s s g es poten ial i ferences in e io ogies o the io s s bg o ps of ildren. Furt e in es iga io s in o the ai mo p o ogy ill he p o el i ate he a ses for an signifi ance of hese s b le ifferences.

ACKNOWL DGEM N S

W wa e a S R W9 ZS 8 N a e
S F a

LITERATURE C T D

1 Fa a 199 e e ea a a e N w Y Ra e e

2 e e a 2 5 e a e ee e a e ea e a e 3 M a e a e J Me e e 138 2 7 2 3

3 e e S R e e J 2 1 a a a a e a a a a a e a a a Ha R e